Research Square

Preprints are preliminary reports that have not undergone peer review.
They should not be considered conclusive, used to inform clinical practice,
or referenced by the media as validated information.

Synthesis, Diffusion technical in a liquid-liquid, Crystal Structure, Hirshfeld Surface interactions, theoretical studies, Assessment of Antioxidant, Enzyme Inhibitor Properties and Docking simulation of nickel(II) complex tetradentate Schiff base

Nadir Ghichi
nadirgh82@hotmail.com

University of Mentouri Brothers
Bilel Mezhoud
University of Mentouri Brothers
Ahmed Abderrahim Yahiaoui
Superior Normal School of technological (ENSET)
Redouane Lemoui
Unit for Valorization of Natural Resources, University of the Brothers Mentouri
Muhammad Ashfaq
University of Sargodha
Mehran Feizi-Dehnayebi
Suleyman Demirel University
Helen Stoeckli-Evans
University of Neuchâtel
Aurélien Crochet
University of Sargodha
Adnan Cetin
Van Yuzuncu Yil University
Fikret Türkan
Iğdır Üniversitesi
Ercan Oğuz
Iğdır Üniversitesi
Khalil Sahra
University of Jijel
Ramzi Maadadi
Scientific and Technical Research Center for Physicochemical Analysis CRAPC Bou-Ismaïl
Hacene Bendjeffal
Superior Normal School of technological (ENSET)
Smail Khelili
University of Jijel
Hasan Küçükbay
İnönü University
Hocine Merazig
University of Mentouri Brothers

Research Article

Keywords: Shiff base, Crystal structure, Nickel, HS, Antioxidant activity, enzyme inhibitory

Posted Date: April 6th, 2026

DOI: https://doi.org/10.21203/rs.3.rs-9245501/v1

License: This work is licensed under a Creative Commons Attribution 4.0 International License. Read Full License

Additional Declarations: No competing interests reported.

Abstract

In the present work, we report the synthesis, characterization, biological studies of the nickel(II) complex **NiL** derived from N_2O_2 tetradentate Schiff base ligand 2,2'-{(1*E*,1'*E*)-[1,2-phenylenebis(azanylylidene)]bis(methanylylidene)}bis(5-benzyloxy)phenol **L**. We used ^{1}H, FT-IR, for characterization, and the structure of the complex was determined by single crystal X-Ray crystallography. Hirshfeld surface analysis and two-dimensional fingerprint plots of **NiL** were calculated to quantify the interatomic interactions present in the crystal. On the other hand, The molecular structure of complex was investigated using DFT calculations at the DFT/B3LYP/6-311g (2d,2p)/LANL2DZ level. The interaction between the complex **NiL** with related target protein (3WZE) receptor was examined using docking experiments. Additionally, the antioxidant activity of the NiL was evaluated by two antioxidant activity assays (DPPH; ABTS) and the enzyme inhibitory potential of the **NiL** compound was investigated against key enzymes involved in neurodegenerative (acetylcholinesterase (AChE), the α-Glycosidase inhibitory and GST inhibitory activity.

1. Introduction

Schiff bases play a crucial role in synthesizing various industrially and physiologically beneficial chemicals through closure, cycloaddition, and replacement reactions [1], Schiff bases are ligands that have a There are imines in the RC group (– RC = N–) created by reacting primary amines (R–NH2) with compounds containing a carbonyl group (RCOR'). The R and R'groups can be there are either alkyls or aryls. The range of services provided by Schiff bases is extensive alternatives that can substitute for and be suitable for bridged N, N', or unbridged. Generally, a Schiff base consists of donor atoms. The presence of oxygen can be associated with NO or N_2O_2 substituted by nitrogen, it can also be present in a molecule containing sulphur or selenium [2], Cancer poses significant challenges globally due to its tendency to develop drug resistance and inadequate response to cytotoxic treatments [1], Schiff bases are an essential class of organic compounds with a wide variety of applications in many fields, such as analytical, biological and inorganic chemistry. Some of these compounds act as corrosion inhibitors and are used as catalysts in polymers and dyes. Furthermore, Schiff bases have gained importance in medicinal and pharmaceutical fields due to their broad spectrum of biological activities like antimicrobial, antifungal, antiviral, anti-inflammatory, analgesic, anticonvulsant, antitubercular, anticancer, antioxidant, anthelmintic, antimalarial and so forth [3], Nickel ion plays an important role in the biological systems, the complexes of nickel are still attract considerable attention because it can exhibit several oxidation states and such complexes have a strong role in bioinorganic chemistry and redox enzyme systems [4], Molecular docking is a method utilized to forecast and examine the interaction between a drug or chemical and a target protein. This computer-based method allows us to model how the drug interacts with the target protein at a tiny level, helping us understand their interactions and evaluate the potential effects of the drug, Computational analysis facilitates drug development from both synthetic and natural molecules, particularly phytochemicals derived from medicinal plants, by predicting the potential therapeutic effects of these substances. Molecular docking is the most prevalent computer approach used in structure-based drug design for predicting protein-ligand interaction sites and their binding affinity scores [5].

In the present study, we aimed at synthesizing and characterizing the **NiL**, see Scheme 1. Its structure was confirmed by XRD crystal structure analysis, and IR and NMR spectroscopies. The antioxidant activity of the synthesized compound was evaluated. Quantum chemical calculations have also been carried out for the estimation of the geometrical parameters, and properties of the title compound. The synthetized compound has been tested for their ADME-T, molecular docking, antioxidant activities and their enzyme inhibition activities.

2. Experimental

2.1. Materials and methods

All the chemicals and solvents were purchased from, Sigma Aldrich and were used without further purification. The Merck Company supplied all reagents and solvents used in this study, which were utilized without purification. The FT-IR spectrums were carried out by the ATR method using a Perking Elmer L1600-400 Spectrum Two spectrophotometer.. The ^{1}H NMR spectra

was recorded on a Bruker DRX-400 high performance digital FT-NMR spectrometer (400 and 100 MHz respectively) using TMS as an internal standard.

2.2. XRD and HSA computing details

Data collection: Stoe STADIVARI diffractometer; cell refinement: X-AREA [6]; data reduction: X-AREA and X-AREA LANA [6]; program used to solve structure: SHELXS97[7]; program used to refine structure: SHELXL2018/3 [8]; molecular graphics: Mercury [9]; software used to prepare material for publication: PLATON [10], SHELXL2018/3 [8]. Crystal data, data collection and structure refinement details are summarized in Table 1 and selected geometric parameters are presented in Table 2. The C-bound H atoms were positioned geometrically (C–H = 0.94–0.98 Å) and refined with U_{iso} (H) = 1.2U_{eq} (C).

Table 1
Single crystal XRD details

CCDC	**2436504**
Chemical formula	$C_{34}H_{26}N_2NiO_4$
M_r	585.28
Crystal system, space group	Monoclinic, $P2_1/c$
Temperature (K)	250
a, *b*, *c* (Å)	6.1728 (1), 29.9870 (9), 14.5398 (3)
β (°)	93.339 (2)
V (Å^3)	2686.80 (11)
Z	4
Radiation type	Cu *K*α
μ (mm^{-1})	1.40
Crystal size (mm)	0.96 × 0.33 × 0.02
Diffractometer	STOE STADIVARI
Absorption correction	Multi-scan (*X-RED32* & LANA; Stoe & Cie, 2024)
No. of measured, independent and observed [$I > 2\sigma(I)$] reflections	48864, 4683, 4309
R_{int}	0.023
$(\sin \theta/\lambda)_{max}$ (Å^{-1})	0.599
$R[F^2 > 2\sigma(F^2)]$, $wR(F^2)$, S	0.042, 0.120, 1.06
No. of reflections	4683
No. of parameters	371
H-atom treatment	H-atom parameters constrained
$\Delta\rho_{max}$, $\Delta\rho_{min}$ (e Å^{-3})	0.32, −0.54

Table 2
Hydrogen-bond geometry (Å, º).

D—H···*A*	*D*—H	H···*A*	*D*···*A*	<(*D*—H···*A*)°
C18—H18···O1^{i}	0.94	2.60	3.426 (3)	148
Symmetry code: (i) *x* − 1, −*y* + 1/2, *z* − 1/2.				

2.3 DFT and topology insights

The molecular structure of the Ni(II) complex was constructed using GaussView 6 and fully optimized with the Gaussian 09W program package [11]. Geometry optimization was carried out within the framework of density functional theory (DFT) using the B3LYP functional. The 6-311g (2d,2p) basis set was applied to the lighter atoms, while the LANL2DZ basis set was employed for the Ni center. Vibrational frequency calculations were performed at the same level of theory in conjunction with the geometry optimization, confirming that the optimized structure corresponds to a true minimum on the potential energy surface, as evidenced by the absence of imaginary frequencies. Key electronic properties of the complex, including molecular electrostatic potential (MEP) surfaces, HOMO and LUMO energy levels, and global quantum chemical reactivity descriptors, were evaluated at the DFT/B3LYP/6-311g (2d,2p)/LANL2DZ level of theory. In addition, the reduced density gradient (RDG) isosurface and the corresponding RDG scatter plots were computed and analyzed to further characterize noncovalent interactions within the complex.

2.4 ADME-T and Molecular docking modeling

ADME-Tox properties of the Ni(II) complex were predicted using the OSIRIS DataWarrior platform. Based on the ADME-Tox profile, molecular docking studies were carried out to evaluate the potential anticancer activity of the complex. For this purpose, a cancer-related protein receptor (PDB ID: 3WZE) was selected as the biological target. The crystallographic structure of the receptor, with a resolution of 1.90 Å, was obtained from the Protein Data Bank (RCSB PDB). Docking calculations were performed using AutoDock Tools 1.5.6 [12] and AutoDock 4.2 [13]. The ligand structure used in the docking simulations corresponded to the DFT-optimized geometry obtained at the B3LYP/6-311g (2d,2p)/LANL2DZ level of theory. Prior to docking, the protein structure was prepared by removing crystallographic water molecules and co-crystallized ligands, followed by the addition of polar hydrogen atoms and Kollman charges. The prepared receptor was then converted to pdbqt format. A grid box of 110 × 110 × 110 points with a grid spacing of 0.375 Å was defined to cover the active binding region of the 3WZE target. Docking runs were conducted using the Lamarckian Genetic Algorithm (LGA). The resulting docking conformation was converted to PDB format using UCSF Chimera 1.17.3, and the interacted complex was analyzed and visualized with Discovery Studio Visualizer 4.1.

2.5. Antioxidant activity assays and Enzyme Inhibitor protocol

In this study, the biochemical and antioxidant activities of the synthesized **NiL** complex was comprehensively evaluated using multiple complementary methods. Antioxidant potential was assessed through 1,1-diphenyl-2-picrylhydrazyl (DPPH) and 2,2'-azino-bis(3-ethylbenzothiazoline-6-sulfonic acid) (ABTS) radical scavenging assays, while enzymatic inhibitory effects were measured against acetylcholinesterase (AChE), glutathione S-transferase (GST), and α-glucosidase (α-Gly). All assays were performed spectrophotometrically using a standard UV-Vis spectrophotometer and quartz cuvettes. Test compounds were prepared in appropriate solvents, including methanol for DPPH and ABTS assays and phosphate buffer solutions for enzymatic assays. Substrates used included DPPH, ABTS, acetylthiocholine iodide (ACHI) with 5,5'-dithiobis-(2-nitrobenzoic acid) (DTNB) for AChE, reduced glutathione (GSH) with 1-chloro-2,4-dinitrobenzene (CDNB) for GST, and p-nitrophenyl-α-D-glucopyranoside (pNPG) for α-Gly. Donepezil (DNP), acarbose (ACB), and ethacrynic acid (INN), used as reference inhibitors, were commercially purchased. All reagents, substrates, and enzymes were purchased commercially from Sigma-Aldrich (St. Louis, MO, USA) to ensure analytical grade quality and consistency.

2.5.1 α-Gly Inhibitory Activity

The α-Gly inhibitory activities of the synthesized **NiL** complex was determined spectrophotometrically by monitoring the hydrolysis of pNPG. The assay was conducted in 0.1 M phosphate buffer (pH 6.9) using α-Gly (EC 3.2.1.20, from Saccharomyces cerevisiae) at 25°C under controlled incubation conditions. Test compounds were initially dissolved in DMSO and diluted with buffer to obtain appropriate concentration ranges for IC_{50} determination, while ensuring that the final DMSO concentration in the reaction medium did not exceed 1% (v/v) to avoid solvent-related interference. Following pre incubation of the enzyme with the ligand or metal complex, the reaction was initiated by the addition of pNPG and terminated after a defined incubation period by adding Na_2CO_3. The formation of *p*-nitrophenol was quantified by measuring absorbance at 405 nm using a microplate spectrophotometer. Percentage inhibition was calculated relative to a control assay performed in the absence of inhibitor, and IC_{50} values were determined from the concentration inhibition profile. All measurements were carried out spectrophotometrically with at least three independent repetitions to ensure experimental reliability. The α-Gly activity was following the method of Kim et al. (2005) with minor modifications for the **NiL** complex [14–15].

2.5.2 GST Inhibitory Activity

The inhibitory activity of the synthesized **NiL** complex against GST was determined spectrophotometrically based on the enzymatic conjugation of reduced GSH with CDNB [16]. The assay was carried out in 0.1 M phosphate buffer (pH 6.5) at controlled temperature, using a standard quartz cuvette in an UV-Vis spectrophotometer. The reaction mixture contained GST enzyme, GSH, CDNB, and the test compound at five different concentrations. After pre-incubation of the enzyme with the inhibitor for 5 min, the reaction was initiated by the addition of substrates. The formation of the GS-CDNB conjugate was monitored as an increase in absorbance at 340 nm over a defined time interval. Each measurement was repeated at least three times to ensure reproducibility. IC_{50} values were determined directly from the concentration response data obtained from absorbance measurements at each inhibitor concentration. The methodology of the study was fundamentally based on Habig et al. [17], but it was carried out with adaptations incorporating insights from recent references [18–20].

2.5.3 AChE Inhibitory Activity

The inhibitory activity of the synthesized **NiL** against AChE (EC 3.1.1.7) was evaluated spectrophotometrically using the Ellman method [21]. The assay is based on the hydrolysis of ACHI by AChE, producing thiocholine, which reacts with DTNB to form a yellow 5-thio-2-nitrobenzoate anion detectable at 412 nm [22]. The reaction mixture contained AChE, ATCI, DTNB, and the test compound at five different concentrations. After pre-incubation of the enzyme with the inhibitor for 5 min at 25°C, the reaction was initiated by substrate addition. Absorbance changes were recorded over a defined period using a UV-Vis spectrophotometer in a standard quartz cuvette. Each measurement was repeated at least three times to ensure reproducibility. The methodology was fundamentally based on the classical protocol described with minor modifications for the evaluation of synthetic compound by Ellman et al. IC_{50} values were determined directly from the concentration response data obtained from absorbance measurements, providing a quantitative assessment of AChE inhibition consistent with modern enzyme inhibitory studies [23–25].

2.5.4 Antioxidant Activity Assays

2.5.4.1 DPPH Radical Scavenging Assay

The radical scavenging activity of the synthesized **NiL** complex was assessed using the DPPH assay, a spectrophotometric method that estimates the ability of test compounds to donate hydrogen atoms or electrons to neutralize free radicals. A methanolic solution of DPPH was prepared at a defined concentration and mixed with varying concentrations of the test compounds. After a fixed incubation period in the dark at room temperature, absorbance values were measured at 517 nm using an UV-Vis spectrophotometer. The decrease in absorbance relative to a control reaction without test compound reflects the radical scavenging capacity of the **NiL** complex. This assay protocol is based on established spectrophotometric DPPH methodologies and measurements were performed in at least three independent repetitions to ensure reproducibility [26, 27].

2.5.4.2 ABTS Radical Cation Decolorization Assay

Antioxidant activity was further evaluated using the ABTS radical cation decolorization assay. The ABTS radical cation ($ABTS^{\bullet+}$) was generated by reacting ABTS with an oxidizing agent, typically potassium persulfate, to form a stable blue-green chromophore. This radical solution was diluted to achieve an appropriate absorbance at 734 nm before mixing with the test compounds at varying concentrations. After incubation for a defined period, the reduction in absorbance was recorded at 734 nm [28, 29]. The extent of absorbance reduction indicates the ability of the test compounds to quench the $ABTS^{\bullet+}$ radical. As with the DPPH assay, each condition was measured at least three times to confirm analytical reliability.

3. Synthesis and crystallization

3.1. Synthesis of ligand L 2, 2'-{(1*E*,1'*E*)-[1,2-phenylenebis(azanylylidene)]bis(methanylylidene)}bis(5-benzyloxy)phenol [30]

1,2-Diaminebenzene (0.027 g) and 4-benzyloxy-2-hydroxybenzaldehyde (0.1141 g) in ethanol (15 ml) were refluxed for 1 h, then the solvent was evaporated in vacuo. The residue was recrystallized from ethanol, yielding yellow block-like crystals of the title compound on slow evaporation of the solvent. The purity of the compound was characterized by its NMR spectrum (250 MHz, $CDCl_3$). The azomethine proton appears in the 8.5–8.7 p.p.m. range, while the imine bond is characterized in the ^{13}C RMN spectrum with the imine C and OH signals in the range 162.23–163.34 p.p.m. 1H NMR: δ = 6.5–7.6 (m, 12H; H-ar), δ = 13.7 (s, 1H; OH), δ = 5.1 (s, 1H; CH2–O). 13C NMR: 70.15, 120.33, 127.30, 127.64, 128.26, 128.75, 142.32, 162.23, 163.33, 163.34.

3.2. Synthesis of complex NiL

A mixture of Ni(II) acetate (1 equivalent) and ligand solution (1équivalent) dissolved in methanol and dichloromethane. A solvent is used as an insulator between the ligand and the nickel metal. The reaction and complex crystallization process takes place using the liquid-liquid diffusion technical, in a glass tube with a diameter between 2 millimeters (like NMR tubes) and 10 millimeters. For a few days, needle orange crystals were formed in Yield, FT-IR, v(cm^{-1}), 3354; 1610; 1572; 1271–1021; 598(str). **^{1}H NMR (400 MHz, DMSO-d_6)**: δ 8.64 (s, 2H, 2CH = N), 6.34–6.40 (m, 6H, H_{Ar}), 7.23–7.47 (m, 12H, H_{Ar}), 7.95–78.10 (m, 2H, H_{Ar}), 5.11 (s, 4H, $2OCH_2$).

4. Results and discussion

4.1 Analytical data

4.1.2 Supporting evidence from NMR, IR

4.1.2.1 IR analysis

The experimental IR spectrum (see Fig. S1 in supplementary information) revealed characteristic bands corresponding to the functional groups present in the molecule of synthesized compound. The FT-IR spectrum of the Ni(II) complex exhibits characteristic bands that confirm coordination between the Schiff base ligand and the metal center. A broad band observed at 3354 cm^{-1} is attributed to the phenolic v(O–H) vibration, showing reduced intensity and broadening, which suggests partial deprotonation and the involvement of the phenolic oxygen atom in coordination. The azomethine v(C = N) band appears at 1610 cm^{-1} at a lower wavenumber region, indicating coordination through the imine nitrogen due to electron donation to the Ni(II) center and a consequent decrease in C = N bond order. The band at 1572 cm^{-1} corresponds to aromatic v(C = C) vibrations, confirming the preservation of the aromatic framework upon complex formation, while the absorptions in the 1271–1021 cm^{-1} region are assigned to v(C–O) and v(C–N) vibrations, supporting the retention of the conjugated Schiff base structure. Importantly, the appearance of a band at 598 cm^{-1}, assigned to v(Ni–O) and v(Ni–N) stretching modes, provides direct evidence of metal–ligand bond formation. These spectral features indicate that the ligand acts as a bidentate (N,O) donor,

forming a four-coordinate Ni(II) complex that is likely to adopt a square-planar geometry, consistent with typical Schiff base nickel(II) complexes.

4.1.2.2 NMR analysis

The ^{1}H NMR spectrum of the complex exhibits several characteristic signals reflecting the different electronic environments of the protons. The hydrazone –CH = N– protons appear as a singlet at δ 8.64 ppm with an integration of 2H, indicating the effect of the metal on the electrons in this position. The $–OCH_2–$ benzyl protons appear as a singlet at δ 5.11 ppm with an integration of 4H, corresponding to a relatively stable environment, distant from the direct influence of the metal. Aromatic protons appear as multiplets in several regions: δ 6.34–6.40 ppm (6H), δ 7.23–7.47 ppm (12H), and δ 7.95–8.10 ppm (2H), reflecting the gradual influence of nickel on the electronic environment of aromatic protons close to the coordination site, with some signals broadened and shifted downfield for protons near the metal, while distant protons remain in the moderate chemical shift range.

4.2 XRD, HAS and Voids analysis part of NiL

The molecular structure is a Schiff base nickel complex (Table 1) in which Schiff base ligand acted as a tetradentate ligand Fig. 1. Ni-center is coordinated by two deprotonated phenolic O-atoms and two imino N-atoms of the Schiff base ligand. Ni-N bond lengths are slightly larger than Ni-O bond lengths and bond angles containing nickel as a central atom range from 83.96 (6) to 177.55 (8)°(Table S1 in supplementary information). The value of structural parameter for the present case is 0.04 pointing out that the coordination geometry is slightly non-ideal square planar. Ni-center is deviated by 0.0108 Å towards atom N2 from the RMS plane composed of the coordinating atoms. Two out of three chelation rings formed by the coordination of ligand with Ni-center are puckered while six-membered ring containing N1 is not puckered. Best puckered description for the five-membered puckered ring is “envelope on Ni1”. Schiff base ligand adopted such a conformation that the twist among similar atomic rings on both sides of Ni-center is not same. The dihedral angle of the ring (C8-C13) with rings (C1-C6) and (C15-C20) is 73.6 (8)°, 14.1 (1)°, correspondingly. The dihedral angle of the ring (C22-C27) with rings (C29-C34) and (C15-C20) is 63.1 (8)°, 10.9. (1)°, correspondingly. Molecules are linked via C-H · · · O bonding in the form of infinite C(7) chains [31] that extend along *c*-axis (Fig. 2, Table 2). The crystal packing is further stabilized by π · · · π and C-H · · · π interactions (Fig. 3). These interactions form molecular chains along a-axis. For π · · · π interactions, inter-centroid separation is less than 4 Å and for C-H · · · π interactions, H · · · π distance is 2.63 Å. As per Cambridge structure database, three nickel Schiff base complexes are reported in which benzyl groups present at both ends of present structure is replaced by hydrogen with reference codes FUGCUG [32], POFFOG [33] and POFFOG01 [34]. These reported structures are solvated as FUGCUG has methanol solvent molecule while POFFOG and POFFOG01 are polymorph of each other containing water as solvent molecule. The closest related reported structure has reference code UTIBOP [35] in which instead of benzyl groups, n-decamethylene groups are present. In all these reported structures, coordination geometry around Ni-center is square planar. Bond lengths and bond angles of present structure are consistent with corresponding ones in these reported structures.

Hirshfeld surface analysis has established itself as an important tool in crystal engineering and material design owing to its clear representation of the way molecules interact in a crystal [36]. This mapping of close-contact regions makes it easier for researchers to understand packing efficiency and stability in solid-state systems [37]. This technique is applied in pharmacy and medicine to support the prediction of drug-receptor fit, behavior of crystal forms, and intermolecular recognition. To investigate interatomic contacts, their spatial arrangement and contribution in supramolecular organization stability, Hirshfeld surface analysis [36] is performed for the present compound via Crystal Explorer v. 21.5 [38]. Hirshfeld surface constructed by using normalized distance make it possible to recognize contacts based of their strength. Surface is composed of red, white and blue regions to show short, equal and longer contacts, correspondingly [36, 39]. Red spot on the surface of the molecule around particular carbon and hydrogen atoms indicate that these atoms are involved in making short-range interactions, name of contacts is shown in Fig. 4a. For understanding and validation of π · · · π interactions, Hirshfeld surface is plotted over shape index for present compound. Alternating red and blue triangle-like patterns on the surface around certain rings show that those units participate in π · · · π stacking interactions (Fig. 4b). 2D fingerprint plots offer a compact visual summary of all the intermolecular contacts in a crystal that allow the researcher to identify the interactions which dominate the solid-state molecular organization [40–42]. For present compound, H · · · H interactions have highest contribution in crystal packing

although these interactions are repulsive in nature (Fig. 4c). Following to that interaction, next three top contributor for H · · · C, H · · · O and C · · · C with percentage contribution of 32.7%, 11.8% and 4.9%, correspondingly (Figs. 4d-4f).

Voids in crystal are important to explore as a structure with less empty space has a greater resistance to deformation, while larger voids can create weak points that may lead to mechanical failure. These vacant regions which are not solvent accessible can be used to make predictions about its toughness, durability, and resistance to stress. Figure 5 shows isosurfaces of voids based on reported methodology [43]. Volume of voids is 302.96 $Å^3$ which corresponds to 11.3% voids. As packing efficiency is high indicating absence of any large cavity and compound is predicted to have good mechanical stability.

4.3 DFT insight

4.3.1 Molecular geometry

DFT methods are routinely applied to predict a variety of molecular properties, including structural parameters, electronic features, and chemical reactivity. In the present study, the geometry of the Ni(II) complex was optimized at the DFT/B3LYP/6-311g (2d,2p)/LANL2DZ level of theory, and the optimized structure is shown in Fig. 6. The reported configuration corresponds to the lowest-energy conformation obtained from the calculations. The total electronic energy of the optimized Ni(II) complex was calculated to be − 3230.67 Hartree, with an associated dipole moment of 3.17 Debye. This relatively moderate dipole moment suggests a degree of lipophilic character, which may facilitate interaction with phospholipid bilayer membranes commonly found in biological systems and could support potential biological activity [44]. The DFT-predicted bond lengths and bond angles are in good agreement with the corresponding X-ray crystallographic data, supporting the reliability of the computational model. The calculations further indicate that the Ni(II) center adopts a square-planar coordination geometry, consistent with the experimental structural findings.

4.3.2 MEP map

The MEP provides a three-dimensional representation of the electrostatic environment of a molecule, reflecting the combined influence of nuclear charges and electron density distribution. MEP analysis is widely used to visualize charge distribution within molecular structures and to identify chemically reactive regions. In particular, it is a valuable tool for predicting potential sites of electrophilic and nucleophilic attack and for assessing overall molecular reactivity [45]. The MEP surface of the Ni(II) complex is presented in Fig. 6, illustrating the molecular shape, size, and spatial charge distribution. In the mapped surface, regions of negative electrostatic potential are shown in red and correspond to electron-rich areas that are more likely to attract electrophiles. These regions are primarily localized around heteroatoms, especially oxygen, where electron density is relatively high. In contrast, positive electrostatic potential regions are represented in blue and indicate electron-deficient sites that are more susceptible to nucleophilic attack [46]. Areas of near-neutral potential are displayed in green [47]. For the Ni(II) complex, the MEP map indicates that the O1 and O3 atoms possess pronounced negative electrostatic potential, identifying them as the most favorable sites for electrophilic interaction.

3.3.3 HOMO and LUMO analysis

Frontier molecular orbitals (FMOs), HOMO and LUMO, are key descriptors for understanding molecular reactivity, kinetic stability, electronic structure, ion detection, and possible biological response [48, 49]. The HOMO is associated with electron-donating ability, whereas the LUMO reflects the electron-accepting character of a molecule. Figure 7 shows the spatial distributions and energy levels of the HOMO, LUMO, $HOMO_{-1}$, and $LUMO_{+1}$ orbitals for the Ni(II) complex, together with the corresponding HOMO-LUMO energy gap (ΔE). The magnitude of this energy gap is commonly used to assess the reactivity and stability of newly synthesized compounds. In general, a smaller HOMO-LUMO gap is correlated with higher chemical reactivity and lower kinetic stability, while a larger gap indicates greater stability and reduced reactivity. For the Ni(II) complex, both the HOMO and LUMO electron densities are mainly localized around the central region of the molecule. The calculated HOMO-LUMO energy gap is 3.28 eV, which is comparable to values reported for related biologically relevant coordination compounds [50, 51]. This moderate gap suggests a favorable balance between stability and reactivity and supports the potential of the complex to participate in electronic and chemical interactions.

4.3.4 Quantum chemical reactivity descriptors

The HOMO energy (E_{HOMO}), LUMO energy (E_{LUMO}), and the corresponding energy gap (ΔE) are important descriptors for predicting molecular reactivity and quantum chemical behavior. These orbital energies can be used to derive several global reactivity parameters, including chemical potential (μ), absolute electronegativity (χ), global hardness (η), global softness (σ), and electrophilicity index (ω). Within the Kohn-Sham DFT framework, these descriptors are commonly estimated using the following relationships (Eqs. 1–5):

$$= -\chi$$

1

$$\chi = \frac{-(E_{HOMO} + E_{LUMO})}{2}$$

2

$$\eta = \frac{E_{LUMO} - E_{HOMO}}{2}$$

3

$$\sigma = \frac{1}{\eta}$$

4

$$\omega = \frac{^{2}}{2\eta}$$

5

The calculated frontier orbital energies and derived global reactivity descriptors for the Ni(II) complex are summarized in Table 3. The computed E_{HOMO} and E_{LUMO} values are − 5.31 and − 2.03 eV, respectively, giving an energy gap of 3.28 eV. From these values, the electronegativity (χ), hardness (η), softness (σ), chemical potential (μ), and electrophilicity index (ω) were obtained as 3.67 eV, 1.64 eV, 0.61 eV^{-1}, − 3.67 eV, and 4.10 eV, respectively. The negative value of the chemical potential indicates that the complex is electronically stable with respect to charge exchange with its environment. The relatively low global hardness (1.64 eV) and corresponding softness suggest a moderate tendency toward chemical reactivity. The calculated electronegativity (χ = 3.67 eV) reflects a favorable electron-accepting capability, particularly in interactions with less electronegative partners, which may promote the formation of polar interactions. In addition, the electrophilicity index (ω = 4.10 eV) indicates a notable capacity to accept electron density, which can be relevant when considering interactions with electron-rich sites in biological macromolecules such as proteins.

Table 3
Quantum reactivity parameters of Ni(II) complex.

parameter	Ni(II) complex
E_{HOMO}	-5.31
E_{LUMO}	-2.03
$\Delta E_{(LUMO-HOMO)}$	3.28
χ	3.67
η	1.64
σ	0.61
μ	-3.67
ω	4.10

4.3.5 NCI-RDG analysis

Noncovalent interaction (NCI) analysis using the reduced density gradient (RDG) provides a detailed visualization of weak intermolecular and intramolecular interactions in molecular systems. The RDG isosurfaces and corresponding scatter plot for the Ni(II) complex are presented in Fig. 8. In the RDG scatter graph, strong attractive interactions, such as hydrogen bonds, are indicated on the left side, steric repulsion on the right, and weak van der Waals interactions in the central region. The RDG isosurface of the Ni(II) complex reveals green-to-red regions between certain C–H···C–H contacts, suggesting weak van der Waals interactions that help stabilize the molecular framework. Additionally, a pronounced red region is observed at the center of the aromatic ring. These red isosurfaces correspond to areas of localized steric or electronic repulsion, which are typical of tightly packed aromatic systems. Overall, the RDG analysis confirms that the Ni(II) complex exhibits a balance of stabilizing weak interactions and localized repulsive regions, providing insight into its conformational stability and potential interaction sites for further biological or chemical investigations.

4.4 ADME-T analysis

The pharmacokinetic and toxicity-related properties of the Ni(II) complex were estimated using the OSIRIS DataWarrior platform, and the predicted parameters are summarized in Table 4. The calculated molecular weight exceeds 500 g/mol, and the compound shows a relatively high lipophilicity (estimated clogP = 6.37), indicating pronounced hydrophobic character. The complex possesses six hydrogen-bond acceptors and no hydrogen-bond donors, suggesting that hydrogen-bonding interactions are mainly acceptor-driven. The predicted drug-likeness value (− 2.32) and overall drug score (0.03) are low, which may be attributed to the high molecular weight and elevated lipophilicity, factors that can negatively influence oral bioavailability according to common drug-likeness criteria. Toxicity risk assessment within the OSIRIS model indicates low risk for mutagenic, tumorigenic, and reproductive effects, whereas a high irritant risk is predicted. Overall, the ADME–Tox screening suggests that while the Ni(II) complex shows favorable profiles in several toxicity categories, its physicochemical properties, particularly high molecular weight and lipophilicity, may limit its drug-likeness in the context of conventional oral drug design. Nevertheless, such characteristics are not uncommon for metal-based complexes and do not preclude potential biological activity, especially in non-oral or targeted therapeutic applications.

Table 4
ADME-Tox analysis of Ni(II) complex predicted by OSIRIS DataWarrior.

Compound	Mw	clogP	HBAs	HBDs	Drug likeness	Mutagenic	Tumorigenic	Reproductive effective	Irritant	Drug score
Ni(II) complex	> 500	6.37	6	0	-2.32	low	low	low	high	0.03

4.5 Docking simulation

Molecular docking simulations are widely used in structure-based drug design to predict ligand-protein binding modes and estimate binding affinities, thereby supporting early-stage drug discovery. In this study, docking analysis was carried out to evaluate the potential interaction of the Ni(II) complex with a cancer-related target protein, vascular endothelial growth factor receptor 2 (VEGFR-2 kinase domain; PDB ID: 3WZE), selected in light of the preliminary ADME–Tox screening results. Docking calculations were performed by exploring the binding of the Ni(II) complex within the active site region of the receptor. The most favorable docking pose, corresponding to the lowest predicted binding free energy, is illustrated in Fig. 9. The calculated binding energy for the best-ranked conformation is − 9.66 kcal/mol, indicating a strong predicted binding affinity between the complex and the receptor binding pocket. Interaction analysis of the top-ranked docking pose shows that the Ni(II) complex forms two hydrogen-bond interactions with residues THR926 and CYS919. In addition, multiple hydrophobic contacts are observed with ARG1032, VAL899, VAL848, LYS868, VAL916, CYS1045, ALA866, LEU840, PHE918, and LEU1035. Several van der Waals interactions further stabilize the complex within the binding site, involving residues ASN923, PHE1047, PRO1057, ASP1056, ASP1058, ARG1051, SER925, GLU885, ASP1046, GLU917, GLY922, and LYS920. The combined contribution of hydrogen bonding, hydrophobic contacts, and van der Waals interactions suggests favorable binding of the Ni(II) complex within the VEGFR-2 active site and supports its potential for further biological investigation.

4.6 Antioxidant activities of the NiL complex

The antioxidant study was conducted to determine the ABTS and DPPH radical scavenging potential of the synthesized **NiL** complex to neutralize free radicals and to evaluate their potential therapeutic value in biological processes associated with oxidative stress. As shown in Table 5, the antioxidant capacities of the synthesized **NiL** complex was evaluated comparatively with standard drugs based on the IC_{50} results obtained from the ABTS and DPPH radical scavenging tests. In the ABTS test, the **NiL** complex (20.14 µg/mL) showed a lower IC_{50} value. However, the values obtained were close to each other. This revealed that **NiL** metal complexation increased radical scavenging activity. It exhibited higher antioxidant activity than the standard drugs ascorbic acid (AA), butylated hydroxytoluene (BHA), and butylated hydroxytoluene (BHT), and these ones displayed lower IC_{50} values of 15.19 µg/mL, 18.78 µg/mL, and 14.68 µg/mL, respectively. In particular, AA (4.68 µg/mL) showed the strongest activity. In the DPPH test, the IC_{50} values of the **NiL** complex (21.60 µg/mL) was found to be quite close to each other. It was observed that complexation did not provide a significant increase in antioxidant activity. BHA, BHT, and AA also showed stronger activity in these DPPH IC_{50} values of 13.69 µg/mL, 15.42 µg/mL, and 13.36 µg/mL, respectively. When the ABTS and DPPH results were evaluated together, it was found that the **NiL** complex showed more advantageous performance in the ABTS system, which is particularly sensitive to the electron transfer mechanism, but was at a similar level in the DPPH system, which is sensitive to hydrogen atom transfer [52, 53]. It can be stated that the synthesized nickel complex possess moderate antioxidant activity and exhibit a lower but significant radical scavenging capacity compared to reference antioxidants.

Table 5
Antioxidant activity of **NiL** complex through ABTS assay and DPPH assay

Compounds	**ABTS activity IC_{50} (µg/mL)**	**σ**	**DPPH activity IC_{50} (µg/mL)**	**σ**
NiL	20.14	2.45	21.60	2.68
*BHA	15.19	3.01	13.69	5.25
*BHT	18.78	3.39	15.42	4.71
*AA	14.68	1.96	13.36	3.66
*Standard antioxidants.				

Meanwhile, when the dose–response curve for DPPH radical scavenging activity is examined in Fig. 10, it is observed that the absorbance values decrease with increasing concentration in all compounds, and correspondingly, the radical scavenging capacity increases. Among the standard antioxidants, AA showed the most pronounced decrease and exhibited the highest antioxidant activity, reaching the lowest absorbance value at a concentration of 60 µg/mL. While BHA also showed strong activity, BHT exhibited a more moderate radical scavenging curve. It is understood that the **NiL** complex exhibited activity close to that of standard antioxidants at low and medium concentrations, but its activity was not as pronounced as AA at high concentrations. It was revealed that the **NiL** complex showed a concentration-dependent increase in activity against the DPPH radical, but its effectiveness lagged behind that of strong standard antioxidants. When examining the dose-response curves for ABTS radical scavenging activity, a significant decrease in absorbance values were observed in parallel with increasing concentrations in all tests, indicating an increase in radical scavenging capacity.

Among the standard antioxidants, AA in particular exhibited the sharpest decline and reached the lowest absorbance values across the entire concentration range, demonstrating the highest antioxidant activity [54, 55]. BHA also exhibited strong activity, while BHT's activity was more limited compared to BHA but still significant. When the synthesized complex was evaluated, the **NiL** complex showed performance close to BHT at low and medium concentrations but lagged behind the strong reference antioxidants. Considering the slope of the curves, it can be said that the **NiL** complex exhibited an antioxidant activity increase sensitive to concentration increase. The antioxidant activities of **NiL** complex was evaluated using DPPH and ABTS radical scavenging assays, and the results demonstrated that the compound exhibited notable radical scavenging abilities in a concentration-dependent manner. The **NiL** complex showed enhanced antioxidant activity, which can be attributed to the coordination of the ligand to the metal center, leading to improved electron delocalization and facilitating electron- or hydrogen-transfer processes. Such an enhancement upon complexation has been widely reported for transition metal complexes, where the metal ion plays a significant role in stabilizing reactive intermediates and promoting redox interactions. In agreement with recent literature reports, the observed activity levels indicate that the metal complex possess effective antioxidant potential and displaying superior performance. These findings suggest that the **NiL** complex may be considered promising candidates as efficient radical scavengers and could have potential relevance for further biological or pharmacological applications [56, 57].

4.7 Enzyme inhibition activities of the NiL complex

The α-Gly, GST, and AChE enzyme inhibition study was planned after the antioxidant activity to reveal the potential biological effects of the synthesized **NiL** complex on neurodegenerative diseases, metabolic disorders, and cellular detoxification mechanisms. Based on the antioxidant activity results, it was predicted that the **NiL** complex exhibiting free radical scavenging capacity have a regulatory or inhibitory effect on enzyme systems associated with oxidative stress, and therefore enzyme inhibition studies were performed. α-glucosidase inhibition shows antidiabetic potential in terms of controlling postprandial hyperglycemia.. GST is one of the key enzymes in the cellular antioxidant defense system and is directly related to oxidative stress. AChE inhibition is therapeutically important in neurodegenerative processes such as Alzheimer's disease. Table 6 shows the IC_{50} values and R^2 values against the α-Gly, GST, and AChE enzymes. When the synthesized **NiL** complex was evaluated against three different enzymes, it was found that the **NiL** complex generally exhibited lower inhibitory properties. In α-Gly inhibition, the **NiL** complex (1.537µM) also demonstrated significantly lower inhibitory activity compared to the ACB was evaluated only for α-Gly and, with an IC_{50} value of 1.553 µM, is nearly equivalent to the **NiL** complex.

Table 6
Enzyme inhibition studies

	AChE		**GST**		**α-Gly**	
	IC_{50} (µM)	**R^2**	**IC_{50} (µM)**	**R^2**	**IC_{50} (µM)**	**R^2**
LN-Ni	**1.627 ± 0.461**	**0.9885**	**1.754 ± 0.382**	**0.9918**	**1.537 ± 0.673**	**0.9979**
***DNP**	2.783 ± 0.317	0.9906	-	-	-	-
****INN**	-	-	4.076 ± 0.649	0.9757	-	-
*****ACB**	-	-	-	-	1.553 ± 0.249	0.9943

Similarly, the **NiL** complex on GST (1.754 μM) is approximately twice as potent. The standard drug INN is one of the weakest inhibitors in the study, with an IC_{50} value of 4.076 μM for GST; both the **NiL** complex are more potent than INN. While the IC_{50} value of the **NiL** complex for AChE is 1.627 μM. This result indicates that the **NiL** complex is more effective in inhibiting AChE. DNP has only been tested for AChE, with an IC_{50} value of 2.783 μM. This value is almost identical to that of the **NiL** complex. Since the Ln042 ligand's IC_{50} value is more than 1.5 times higher, the **NiL** complex has been found to be a stronger inhibitor of AChE than DNP. The **NiL** complex stands out as the most effective inhibitor with lower IC_{50} values in all three enzymes. Compared to standard drugs, the **NiL** complex is understood to be a competitive and potent inhibitor, particularly on AChE and α-Gly, and also exhibits high activity on GST. Figure 11 shows the IC_{50} values of the compounds in the study against the AChE, GST, and α-Gly enzymes.

The low IC_{50} values observed allow for easy comparison of the relative potency of the compounds against the enzymes. **NiL** complex compound exhibited low IC_{50} values on all three enzymes, emerging as the most effective inhibitor. Overall, that complex appeared particularly potent against AChE and αGly. DNP has only been evaluated for AChE, and since this value is higher than that of **NiL** complex, DNP's AChE inhibitory activity is lower than that of **NiL** complex. INN has only been tested on GST and showed a high IC_{50} value; this indicates that INN is the weakest inhibitor for GST in the study. ACB, on the other hand, has only been evaluated for α-Gly and showed a low IC_{50} value for this enzyme, thus demonstrating similar activity to **NiL** complex. It demonstrates that the **NiL** complex compound is a versatile and potent inhibitor, and that among the reference compounds, ACB possesses remarkable inhibitory power against α-Gly. These results clearly reflect the selective and comparative enzyme inhibition profiles of the compounds.

The enzyme inhibition activities of **NiL** complex was evaluated against three target enzymes, and the results clearly demonstrated that the **NiL** complex exhibited superior inhibitory effects compared to the free ligand and the reference standards. Notably, the **NiL** complex showed strong inhibition at micromolar concentrations, indicating a high binding affinity toward the active sites of the enzymes. The enhanced activity observed upon complexation can be attributed to the increased lipophilicity and structural rigidity of the metal complex, which may facilitate better interaction with the enzyme environment and improve its ability to coordinate with key amino acid residues. Additionally, the presence of the Ni(II) center may contribute to stronger electrostatic and coordination interactions within the catalytic region, thereby enhancing the inhibitory efficiency. Similar findings have been reported in recent studies [58, 59], where organic compounds demonstrated significantly improved enzyme inhibition profiles compared to their parent ligands and exhibited effective activity in the micromolar range [60–62].

5. Conclusions

In the present study, tetradentate N_2O_2 schiff base ligand and its Ni (II) complex were synthetized and characterized using various spectral tools such as, FT-IR, NMR. Suitable single crystals for X-ray analysis have been grown by slow evaporation a crystal structure of the complex was obtained. All the major interatomic and intermolecular interactions have been discussed and explained. The crystal packing environment is explored by Hirshfeld surface analysis which indicated that the dominance of the H···H (43.2%) and C···H/H···C (32.7%) interatomic interactions in the crystal lattice. The ADME–Tox screening suggests that while the Ni(II) complex shows favorable profiles in several toxicity categories. To indicate the effect of the title compound NiL against breast cancer mutants by interacting with receptor Protein (VEGFR-2 kinase domain; PDB ID: 3WZE), molecular docking was used by using AutoDock Tools 1.5.6 and AutoDock 4.2 programs. In additional hand, the prepared compound proposed to helpful in the applications for therapy. The evaluation in vitro by DPPH and ABTS revealed a good inhibition. On the other hand, these results clearly reflect the selective and comparative enzyme inhibition profiles of the compounds.

Declarations

Ethics approval and consent for publication

Not applicable.

Consent to participate

Not applicable.

Competing interests

The authors declare no competing interests.

Funding

This work did not receive any specific grant from public, commercial, or not-for-profit funding agencies.

Author Contribution

Authors Contributions Statement Nadir Ghichi Supervisor, elaboration, interpretation, methodology and writingBilel Mezhoud Collaboration and elaborationAhmed Abderrahim Yahiaoui NMR and FT-IR part discussion Redouane Lemoui Collaboration and elaborationMuhammed Ashfeq Crystallography discussionMehran Feizi-Dehnayebi DFT and Docking discussionHelen Stoeckli-Evans Cif File analysis Aurélien Crochet RDX materialAdnan Cetin Biological activityFikret Türkan Biological activityErcan Oğuz Biological activityKhalil Sahra Collaboration and elaborationRamzi Maadadi FT-IR materialHacene Bendjeffal Collaboration and elaborationSmail Khelili Collaboration and elaborationHasan Küçükbay Collaboration and elaborationHocine Merazig RDX technical

Acknowledgement

The principal author thanks the unit of research CHEMS, Chemistry Department, University of Mentouri Brothers, Constantine 1. Algeria, for financing the study, for their collaboration in this research, and all the authors who participle in this work. HSE is grateful to the University of Neuchâtel for their support over the years.

Data Availability

Data is provided within the manuscript or supplementary information files.

References

1. Thakor PM, Patel JD, Patel RJ, Chaki SH, Khimani AJ, Vaidya YH, Chauhan AP, Dholakia AB, Patel VC, Patel AJ, Bhavsar NH, Patel HV (2024) Exploring New Schiff Bases: Synthesis, Characterization, and Multifaceted Analysis for Biomedical Applications. ACS Omega. https://doi.org/10.1021/acsomega.4c02007. 9 35431 – 35448
2. Nidhi S, Rao DP, Gautam AK, Verma A, Gautam Y (2025) Schiff bases and their possible therapeutic applications: A review. Results Chem 13:101941. https://doi.org/10.1016/j.rechem.2024.101941
3. Bennour HAM, Elmagbari FM, Hammouda AN, EL-Ferjani RM, Ben Amer YO, Soliman SM, Jackson GE (2023) Synthesis, characterisation and density functional theory (DFT) studies of a triazine ring with a mixed ligand Schiff base complexes. Results Chem 5:100775. https://doi.org/10.1016/j.rechem.2023.100775
4. Boudraa N, Assabaa R, Ghichi N, Hannachi D, Djedouani A, Kraim Kh, Kashi I, Crouchet A, stoeckli-evans H (2023) Synthesis, crystal structure, theoretical studies and biological evaluation of nickel(II) complex derived from N_2O_2 tetradentate Schiff base. J Mol Struct 1294136398. https://doi.org/10.1016/j.molstruc.2023.136398
5. Ghichi N, Djedouani A, Hannachi D, Yahiaoui AA, Gheraibia S, Abdessemed A, Crochet A, Stoeckli-Evans H, Maadadi R, Merazig H (2025) Synthesis, crystal structure, tautomerism, DFT calculations, nonlinear optical properties, and molecular

docking studies of a novel Schiff base: (Z)-3-(benzyloxy)-6 (((3-hydroxyphenyl)amino)methylene)cyclohexa-2,4-dien-1-one. Discover Chem 2:325. https://doi.org/10.1007/s44371-025-00419-1

6. Stoe & Cie, X-AREA & X-AREA LANA, Stoe & Cie GmbH, Darmstadt, Germany (2022).
7. Sheldrick GM (2008) A short history of SHELX. Acta Cryst Sect A 64:112–122. https://doi.org/10.1107/S0108767307043930
8. Sheldrick GM (2015) Crystal structure refinement with SHELXL. Acta Cryst Sect C 71:3–8. https://doi.org/10.1107/S2053229614024218
9. Macrae CF, Sovago I, Cottrell SJ, Galek PTA, McCabe P, Pidcock E, Platings M, Shields GP, Stevens JS, Towler M, Wood PA (2020) Mercury 4.0: from visualisation to analysis, design and prediction. J Appl Cryst 53:226–235. https://doi.org/10.1107/S1600576719014092
10. Spek AL (2020) check CIF validation ALERTS: what they mean and how to respond. Acta Cryst E76:1–11. https://doi.org/10.1107/S2056989019016244
11. Frisch M, Trucks G, Schlegel HB, Scuseria GE, Robb MA, Cheeseman JR, Scalmani G, Barone V, Mennucci B, Petersson G (2009) gaussian 09, Revision d, vol 01. Gaussian, Inc., Wallingford CT, p 201
12. Garrett M, Huey R, Lindstrom W, Sanner MF, Belew RK, Goodsell DS, Olson AJ (2009) AutoDock4 and AutoDockTools4: Automated docking with selective receptor flexibility. J Comp Chem 30:2785–2791. https://doi.org/10.1002/jcc.21256
13. MGL Tools (2016) 1.5. 6 (ADT)/MGL Tools 1. 6. The Scripps Research Institute, La Jolla, CA, USA
14. Kim YM, Wang MH, Rhee HI (2004) A novel α-glucosidase inhibitor from pine bark. Carbohydr Res 339(3):715–717. https://doi.org/10.1016/j.carres.2003.11.005
15. Mermer A, Keles T, Sirin Y (2021) Recent studies of nitrogen containing heterocyclic compounds as novel antiviral agents: A review. Bioorg Chem 114:105076. https://doi.org/10.1016/j.bioorg.2021.105076
16. Çelik F, Ünver Y, Güler HI, Oğuz E, Türkan F (2025) New methyl/benzyl-1, 2, 4-triazole-3-one Derivatives: Synthesis, Characterization (IR, NMR), Antidiabetic, Anti-Alzheimer, and Molecular Docking Study. J Biochem Mol Toxicol 39(9):e70510. https://doi.org/10.1002/jbt.70510
17. Habig WH, Pabst MJ, Jakoby WB (1974) Glutathione S-transferases: the first enzymatic step in mercapturic acid formation. J Biol Chem 249(22):7130–7139. https://doi.org/10.1016/S0021-9258(19)42083-8
18. Türkan F, Timur Ç (2025) Activity of Doxorubicin Administration on Glutathione S-Transferase, Acetylcholinesterase and Butyrylcholinesterase Enzymes in Rats: Effect of Caffeic Acid. J Inst Sci Technol 15(4):1495–1503. https://doi.org/10.21597/jist.1721484
19. Kotan G, Aras A, Oguz E, Türkan F, Yüksek H (2025) Novel 1-morpholine-3-substituted triazol-5-ones: Synthesis and multi-biological evaluation on HepG2 and U87 cells with SAR and DFT studies. J Mol Struct 143622. https://doi.org/10.1016/j.molstruc.2025.143622
20. Çelik F, Süleymanoğlu N, Ustabaş R, Türkan F, Güler HI, Ünver Y, Kahriman N (2022) New chalcone derivative, ethyl 2-(4-(3-(benzo [b] thiophen-2-yl) acryloyl) phenoxy) acetate: synthesis, characterization, DFT study, enzyme inhibition activities and docking study. J Biomol Struct Dynamics 40(22):12260–12267. https://doi.org/10.1080/07391102.2021.1969287
21. Ellman GL, Courtney KD, Andres V Jr, Feather-Stone RM (1961) A new and rapid colorimetric determination of acetylcholinesterase activity. Biochem Pharmacol 7(2):88–95. https://doi.org/10.1016/0006-2952(61)90145-9
22. Ustabaş R, Çelik F, Süleymanoğlu N, Güler HI, Türkan F, Oğuz E, Ünver Y (2024) 1, 2, 4-Triazol 4-Bromobenzenesulfonates: Synthesis, Characterization (IR, NMR), DFT, Enzym Activities, and Docking Study. Russ J Phys Chem A 98(4):707–719. https://doi.org/10.1134/S0036024424040204
23. Cetin A, Oguz E, Wolińska E, Rozbicki P, Branowska D, Türkan F (2025) Design, Synthesis, and Characterization of Novel Substituted 1, 2, 4-Triazines: Cytotoxic Activity on HepG2 and HT-29 Cell Lines, Enzyme Inhibition, and Molecular Docking Studies. J Biochem Mol Toxicol 39(11):e70591. https://doi.org/10.1002/jbt.70591
24. Bükülmez G, Mert S, Türkan F, Atalar MN, Bursal E, Kasımoğulları R (2025) Synthesis and Biological Activities of Novel Quinazoline–Sulfonamide Derivatives Promising for the Treatment of Alzheimer's Disease. Chem Select 10(12):e202405093. https://doi.org/10.1002/slct.202405093

25. Kocak Y, Oto G, Huyut Z, Alp HH, Turkan F, Onay E (2023) Effects of fluoride on oxidative DNA damage, nitric oxide level, lipid peroxidation and cholinesterase enzyme activity in a rotenone-induced experimental Parkinson's model. Neurol Res 45(11):979–987. https://doi.org/10.1080/01616412.2023.2257452
26. Gulcin I, Alwasel SH (2023) DPPH Radical Scavenging Assay Processes. 11(8) 2248. https://doi.org/10.3390/pr11082248
27. Karageçili H, Yılmaz MA, Ertürk A, Kızıltaş H, Güven L, Alwasel SH, Gulcin I (2023) Comprehensively Revealing the Profile of Pistacia vera L. cv. Siirt Turpentine Antioxidant, Antidiabetic, Anti-Alzheimer, and Antiglaucoma Effects. Records Nat Prod 17(5):918–937. http://doi.org/10.25135/rnp.410.2305.2787
28. Karageçili H, Dirmenci T, Alwasel SH, Gulcin I (2024) Evaluation of the Antioxidant, Antidiabetic and Anti-Alzheimer Effects of Capsella bursa-pastoris. Records Nat Prod 18(6):643–662. http://doi.org/10.25135/rnp.489.2410.3353
29. Balcı N, Aslan K, Ertürk A, Gulcin I (2025) Evaluation of Antioxidant and Enzyme Inhibition Properties of Siran Propolis: Correlations With Phenolic Content Determined by LC-MS/MS. Food Sci Nutr 13(7):e70654. https://doi.org/10.1002/fsn3.70654
30. Ghichi N, Benboudiaf A, DJebli Y, Bensouici C, Merazig H (2018) Crystal structure, Hirshfeld surface analysis and antioxidant capacity of 2,2'-{(1*E*,1'*E*)-[1,2-phenyl- enebis(azanylylidene)]bis(methanylylidene)}bis(5-benzyloxy)phenol. Acta Cryst E74:682–686. https://doi.org/10.1107/S2056989018005832
31. Bernstein J, Davis RE, Shimoni L, Chang NL (1995) Patterns in hydrogen bonding: functionality and graph set analysis in crystals, Angew Chem. Int Ed Engl 34(15):1555–1573. https://doi.org/10.1002/anie.199515551
32. Niu M, Liu G, Wang D, Dou J (2009) A new Schiff base nickel (II) complex:{5, 5'-dihydroxy-2, 2'-[o-phenylenebis (nitrilomethylidyne)] diphenolato} nickel (II) methanol disolvate. Acta Crystallogr Sect E Crystallogr Commun 65(11):m1357–m1357. https://doi.org/10.1107/S160053680904063X
33. Fun HK, Kia R, Mirkhani V, Zargoshi H (2008) {5, 5'-Dihydroxy-2, 2'-[o-phenylenebis (nitrilomethylidyne)] diphenolato} nickel (II) dihydrate. Acta Crystallogr E Crystallogr Commun 64(9):m1181–m1182. https://doi.org/10.1107/S1600536808026093
34. Arola-Arnal A, Benet-Buchholz J, Neidle S, Vilar R (2008) Effects of Metal Coordination Geometry on Stabilization of Human Telomeric Quadruplex DNA by Square-Planar and Square-Pyramidal Metal Complexes. Inorg Chem 47(24):11910–11919. https://doi.org/10.1021/ic8016547
35. Räisänen MT, Nieger M, Slawin AMZ, Leskelä M, Repo T (2011) Two- and three-dimensional packing diagrams of M(salophen) complexes. Cryst Eng Comm 13(14):4701–4708. https://doi.org/10.1039/C0CE00926A
36. Spackman MA, Jayatilaka D (2009) Hirshfeld surface analysis. Cryst Eng Comm 11(1):19–32. https://doi.org/10.1039/B818330A
37. Spackman MA, Byrom PG (1997) A novel definition of a molecule in a crystal. Chem Phys Lett 267(3):215–220. https://doi.org/10.1016/S0009-2614(97)00100-0
38. Spackman PR, Turner MJ, McKinnon JJ, Wolff SK, Grimwood DJ, Jayatilaka D, Spackman MA (2021) CrystalExplorer: A program for Hirshfeld surface analysis, visualization and quantitative analysis of molecular crystals. J Appl Crystallogr 54(3):1006–1011. https://doi.org/10.1107/S1600576721002910
39. Mandal U, Rizzoli C, Chakraborty B, Bandyopadhyay D, Mandal S (2024) Synthesis, crystal structure, Hirshfeld surface analysis and characterization of two new mononuclear Ni(II) complexes. J Mol Struct 1302:137420. https://doi.org/10.1016/j.molstruc.2023.137420
40. Spackman MA, McKinnon JJ (2002) Fingerprinting intermolecular interactions in molecular crystals. Cryst Eng Comm 4(66):378–392. https://doi.org/10.1039/B203191B
41. McKinnon JJ, Jayatilaka D, Spackman MA (2007) Towards quantitative analysis of intermolecular interactions with Hirshfeld surfaces. Chem Comm 53(37):3814–3816. https://doi.org/10.1039/B704980C
42. Isalm ABMN, Habib MA, Hasan MM, Hasan MR, Karim KMR, Mahiuddin M, Yoshida T, Karim MR, Rahman S, Albrithen H, Alodhayb AN, Georghiou PE (2025) Exploration of the synthesis, crystal structure, Hirshfeld surface analysis, binding properties, antibacterial activities, and molecular docking of a Schiff base nickel (II) Complex. J Mol Struct 1322140294. https://doi.org/10.1016/j.molstruc.2024.140294

43. Turner MJ, McKinnon JJ, Jayatilaka D, Spackman MA (2011) Visualisation and characterisation of voids in crystalline materials. Cryst Eng Comm 13(6):1804–1813. https://doi.org/10.1039/C0CE00683A
44. Ragab A, Ammar YA, Ezzat A, Mahmoud AM, Mohamed MBI, El-Tabl AS, Farag RS (2022) Synthesis, characterization, thermal properties, antimicrobial evaluation, ADMET study, and molecular docking simulation of new mono Cu (II) and Zn (II) complexes with 2-oxoindole derivatives. Comput Biol Med 145105473. https://doi.org/10.1016/j.compbiomed.2022.105473
45. Rowhani Y, Reiisi S, Dehnayebi MF (2025) Eugenol-loaded zinc oxide nanoparticles enhance paclitaxel sensitivity in breast Cancer cells: A combined synergistic nanomedicine and theoretical approach. Results Chem 102941. https://doi.org/10.1016/j.rechem.2025.102941
46. Farzandi F, Ziarani GM, Reiisi S, Badiei A, Dehnayebi MF (2025) Tetrazole-based fluorescent probe for sensitive detection of Cu2+: photoluminescence, biological activity, DNA/BSA interaction, and theoretical insights. Results Chem 102992. https://doi.org/10.1016/j.rechem.2025.102992
47. Dehnayebi MF, Ziarani GM, Reiisi S, Farsadrooh M, Panahande Z, Torshizi HM, Akkoc S (2025) Biological evaluations and biomolecular interactions along with computational insights of arylidene isatin hydrazones synthesized using nanocatalyst. Sci Rep 15:142705. https://doi.org/10.1038/s41598-025-26721-7
48. Abu-Dief AM, Mohamed SB, Dehnayebi MF, Omar I, Ayouba MA, Fathalla M, El-Remaily MAEl AAA (2025) Development of benzoxazole-2-yl-guanidine based Cu (II), Co (II), and Ni (II) complexes: Structural features, physicochemical aspects underpinning their pharmaceutical potential supported with theoretical approaches. Biochimica et Biophysica Acta (BBA)-General Subjects. 130893. https://doi.org/10.1016/j.bbagen.2025.130893
49. Ziarani GM, Sh S, Panahande Z, Badiei A, Dehnayebi MF (2026) Fluorescent nanosensor based on Fumed-silica modified with terephthalaldehyde and indandione for selective Hg^{2+} detection: DFT and experimental viewpoints. J Mol Struct 145348. https://doi.org/10.1016/j.molstruc.2026.145348
50. Kundu S, Dehnayebi MF, Akkoc S (2025) Exploring the anticancer potential of novel benzimidazolium salts: synthesis, biological evaluation, DFT perspective, and docking simulation for inhibition of VEGFR2. Biochemical and Biophysical Research Communications. 152472. https://doi.org/10.1016/j.bbrc.2025.152472
51. Mehran FD, Ziarani GM, Lohith TN, Ghareghomi S, Panahande Z, Farsadrooh M, Majidinia M (2025) Probing the biological activity of isatin derivatives against human lung cancer A549 cells: Cytotoxicity, CT-DNA/BSA binding, DFT/TD-DFT, topology, ADME-Tox, docking and dynamic simulations. J Mol Liq 428127475. https://doi.org/10.1016/j.molliq.2025.127475
52. Türkan F, Cetin A, Ustun MA (2025) Pyrimidine Based Inhibitors Targeting Glutathione S-Transferase in Phase II Detoxification: Antioxidant, ADMET, Docking, and Molecular Dynamics Evaluation. J Biochem Mol Toxicol 39(12):e70652. https://doi.org/10.1002/jbt.70652
53. Koçak Y, Yunusoglu O, Huyut Z, Turkan F, INDIAN JOURNAL OF PHARMACEUTICAL EDUCATION AND RESEARCH (2023) Effects of Artemisinin on Anti-epileptogenic, Antioxidant and Cholinesterase Enzymes in Pentylenetetrazole-induced Kindling Model in Mice. 57 (3s):s821–s830. https://doi.org/doi:10.5530/ijper.57.3s.93
54. Turan N, Buldurun K, Türkan F, Aras A, Çolak N, Murahari M, Bursal E, Mantarcı A (2022) Some metal chelates with Schiff base ligand: synthesis, structure elucidation, thermal behavior, XRD evaluation, antioxidant activity, enzyme inhibition, and molecular docking studies. Mol Diversity 26(5):2459–2472. https://doi.org/10.1007/s11030-021-10344-x
55.] Gulçin I, Taslimi P, Aygün A, Sadeghian N, Bastem E, Kufrevioglu OI, Turkan F, Şen F (2018) Antidiabetic and antiparasitic potentials: Inhibition effects of some natural antioxidant compounds on α-glycosidase, α-amylase and human glutathione S-transferase enzymes. Int J Biol Macromol 119:741–746. https://doi.org/10.1016/j.ijbiomac.2018.08.001
56. Türkan F, Atalar MN, Aras A, Gülçin I, Bursal E (2020) ICP-MS and HPLC analyses, enzyme inhibition and antioxidant potential of Achillea schischkinii Sosn. Bioorg Chem 94103333. https://doi.org/10.1016/j.bioorg.2019.103333
57. Türkan F, Taslimi P, Saltan FZ (2019) Tannic acid as a natural antioxidant compound: Discovery of a potent metabolic enzyme inhibitor for a new therapeutic approach in diabetes and Alzheimer's disease. J Biochem Mol Toxicol 33(8):e22340. https://doi.org/10.1002/jbt.22340

58. Demir Z, Cetin A, Oguz E, Kazancioglu MZ, Kazancioglu EA, Türkan F (2025) Urea based derivatives as anticancer agents: cytotoxicity, GST inhibition, molecular docking, ADME, and molecular dynamics approaches. Chem Select 10(35):e02666. https://doi.org/10.1002/slct.202502666
59. Oguz E, Cetin A, Kazancioglu MZ, Kazancioglu EA, Türkan F (2025) Design, Synthesis, and AChE Inhibition of 4-Amino-tetrahydroquinoline Derivatives: Molecular Docking and Biological Evaluation. Russ J Gen Chem 95(11):3435–3445. https://doi.org/10.1134/S1070363225605162
60. Beytur M, Tarmaşır E, Oguz E, Bayrakdar A, Sabancılar I, Akyildirim O, Türkan F, Aras A, Yüksek H (2026) 3-Substituted Triazolone–Benzoate Hybrids: Synthesis, Enzyme Inhibition, Anticancer Activity and ADMET Evaluation by Molecular Docking and Dynamics Studies. Drug Dev Res 87(1):e70222. https://doi.org/10.1002/ddr.70222
61. Cetin A, Türkan F, Oğuz E, Rozbicki P, Wolińska E, Branowska D (2026) Substituted bipyridine-based compounds: Synthesis, enzyme inhibition, anticancer activities and molecular docking studies. Lett Drug Des Discovery 100269. https://doi.org/10.1016/j.lddd.2025.100269
62. Adiguzel R, Türkan F, Yildiko U, Aras A, Evren E, Onkol T (2021) Synthesis and in silico studies of novel Ru (II) complexes of Schiff base derivatives of 3-[(4-amino-5-thioxo-1, 2, 4-triazole-3-yl) methyl]-2 (3H)-benzoxazolone compounds as potent glutathione S-transferase and cholinesterases inhibitor. J Mol Struct 1231:129943. https://doi.org/10.1016/j.molstruc.2021.129943

Scheme

Scheme is available in the Supplementary Files section.

Figures

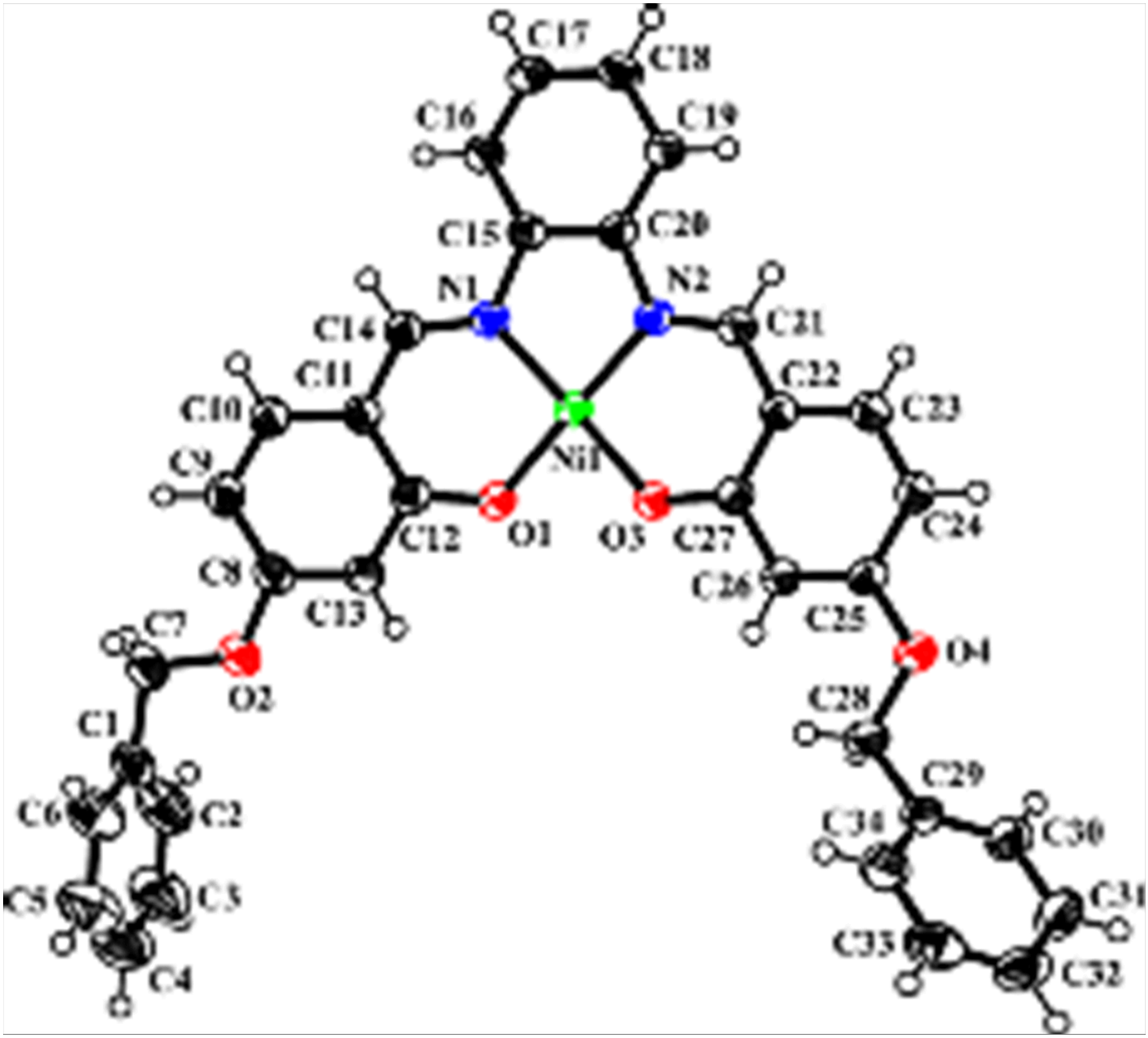


Figure 1

Molecular structure diagram drawn at 50% atomic probability level.

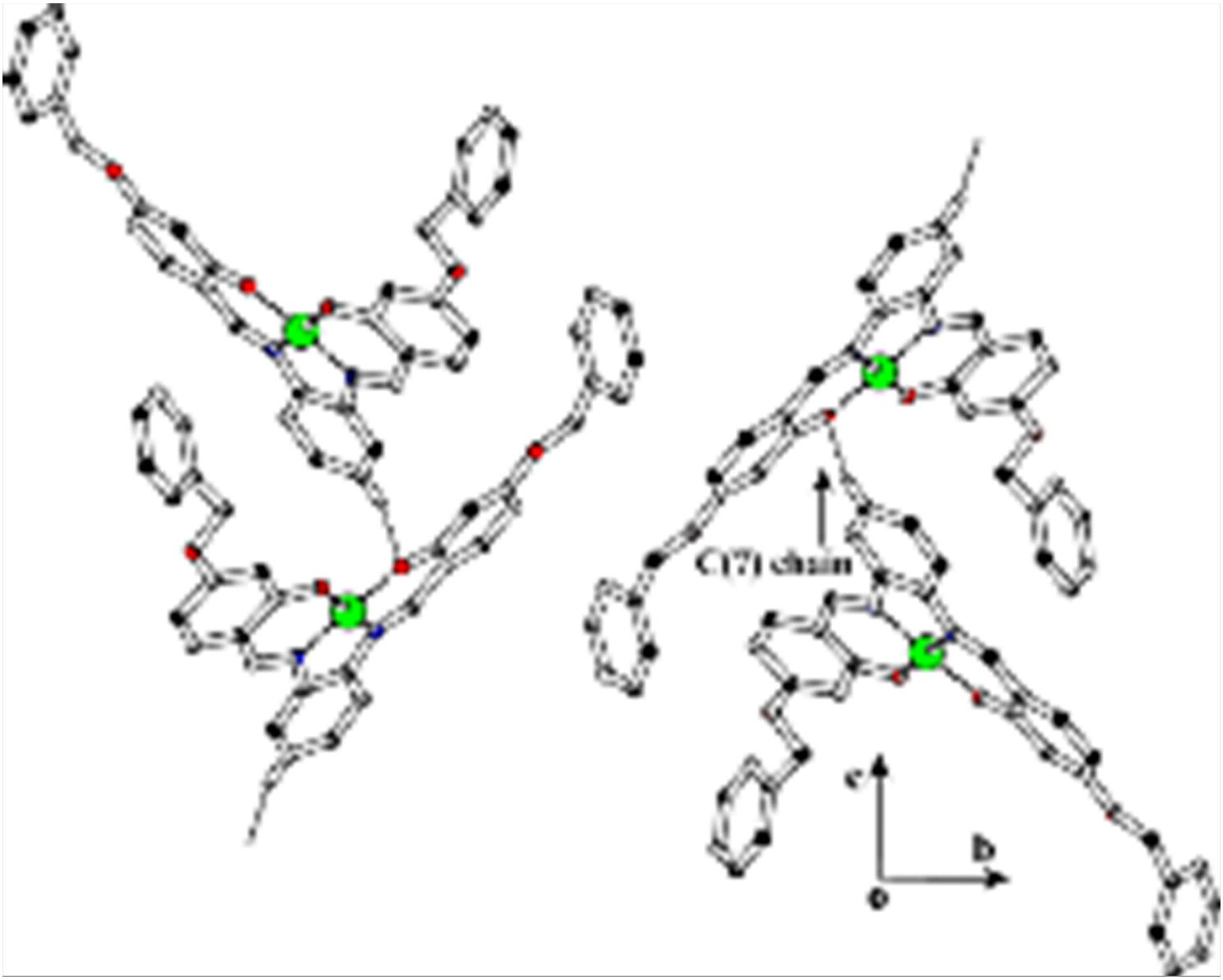


Figure 2

Partial packing diagram showing formation of C(7) chains through C-H···O bonding.

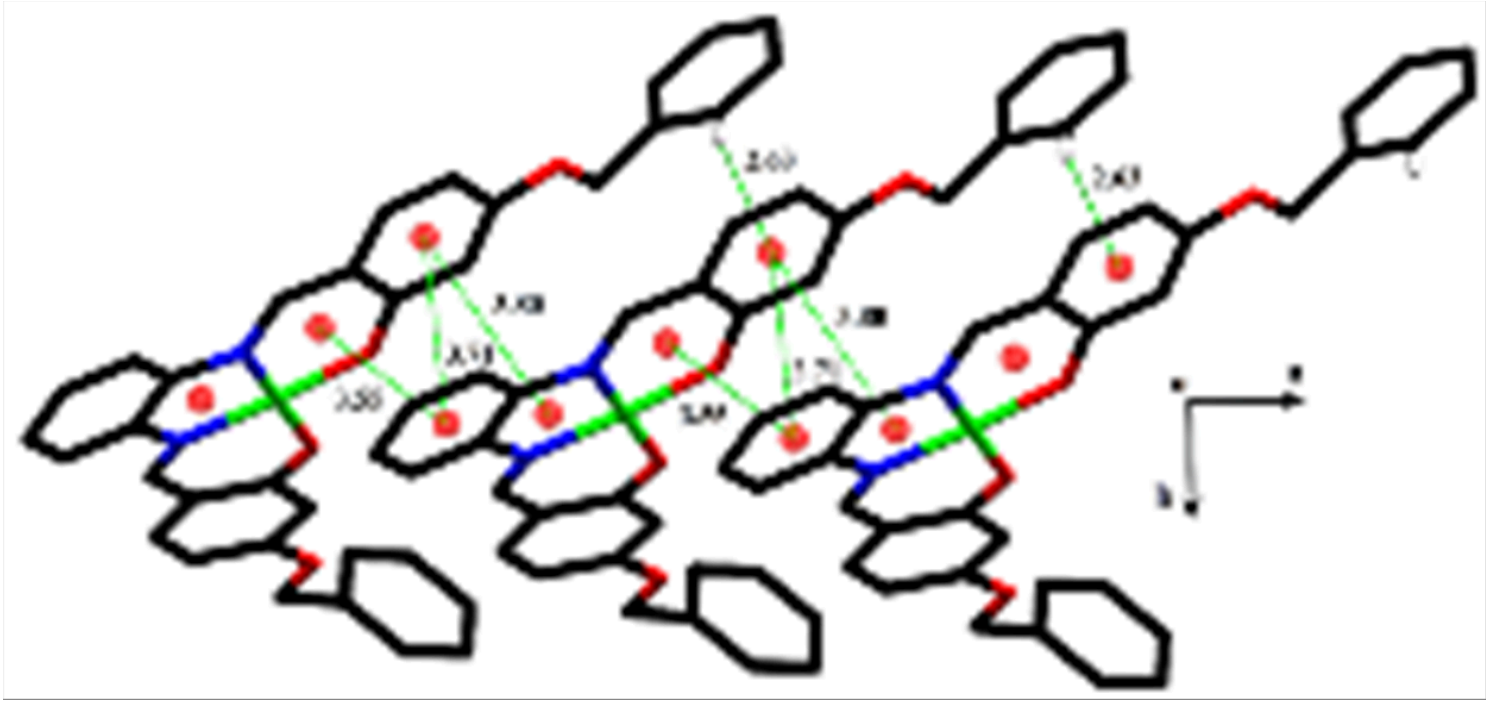


Figure 3

Graphical representation of π···π and C-H···π interactions in In-ni. Selected H-atoms are shown for clarity.

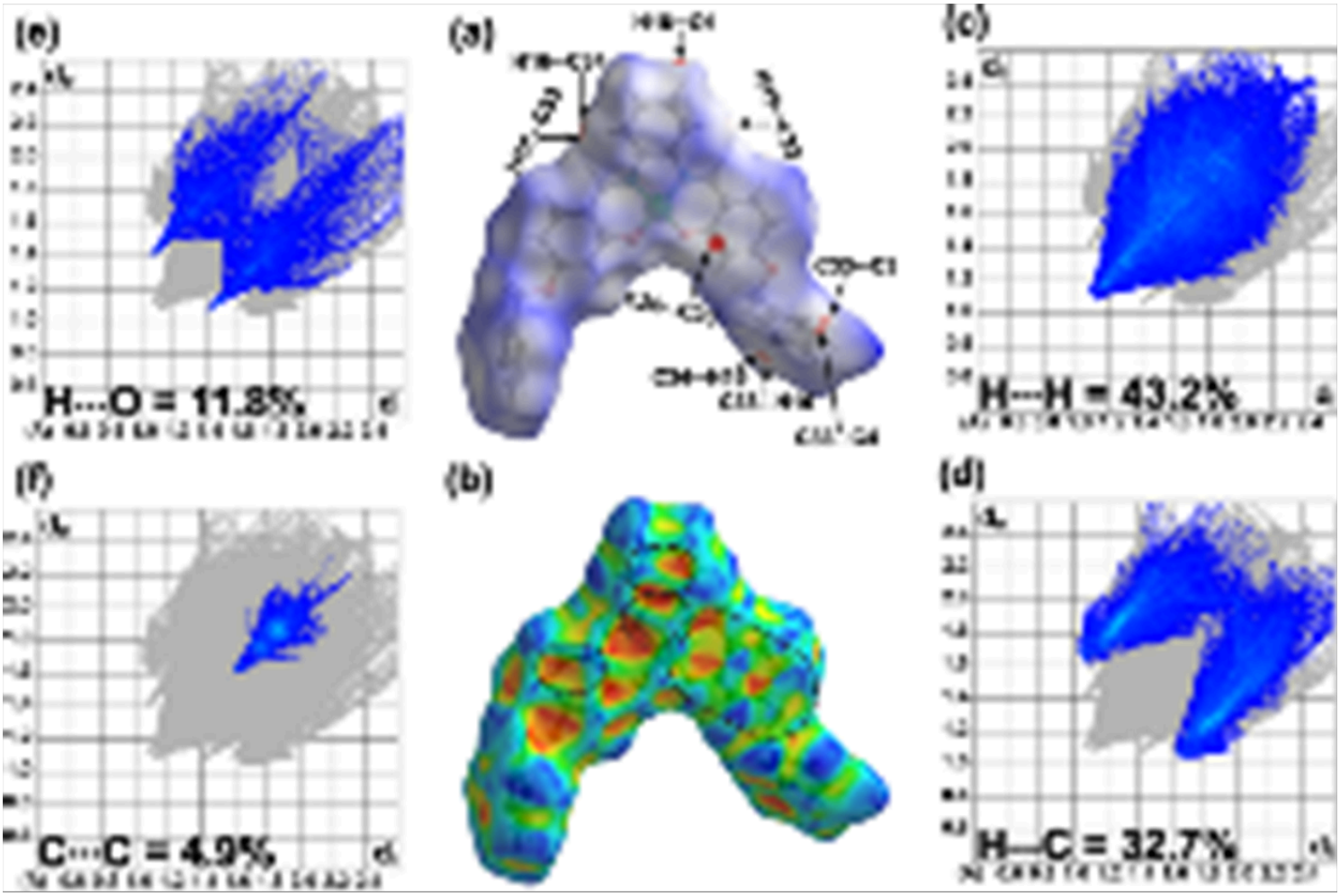


Figure 4

Hirshfeld surface plotted over (a) normalized distances, (b) shape index. (c-f) 2D fingerprint plots of top four contributing contacts.

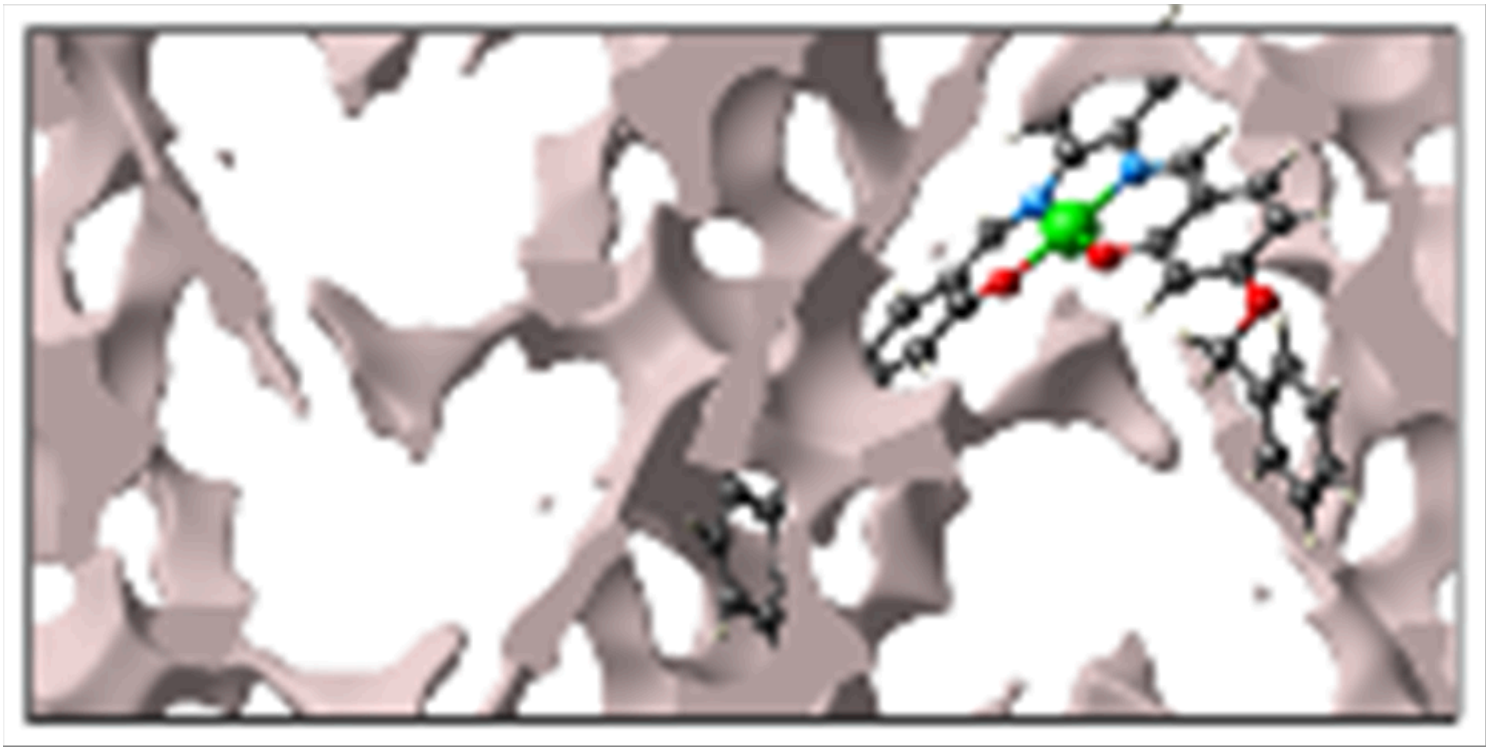


Figure 5

Isosurfaces of voids for **NiL**.

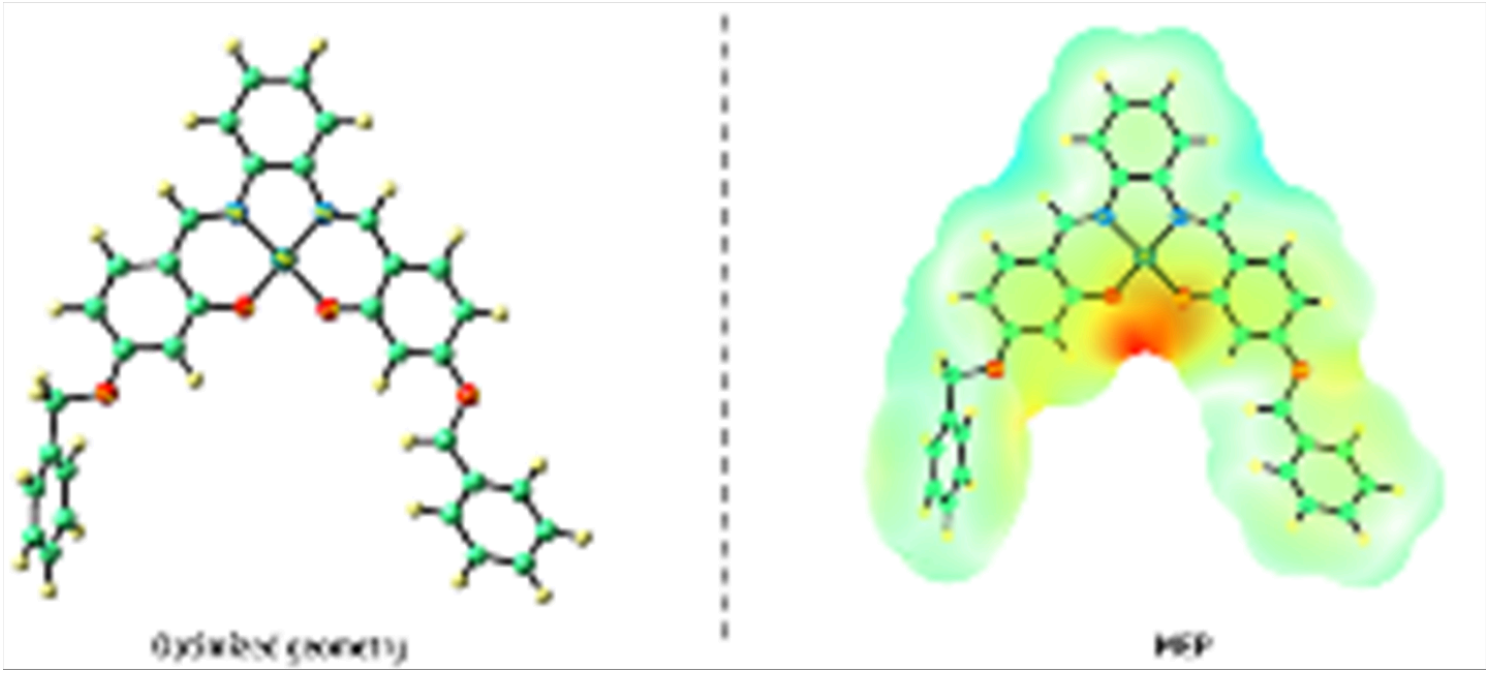


Figure 6

Proposed geometry and MEP map of Ni(II) complex applying DFT insight.

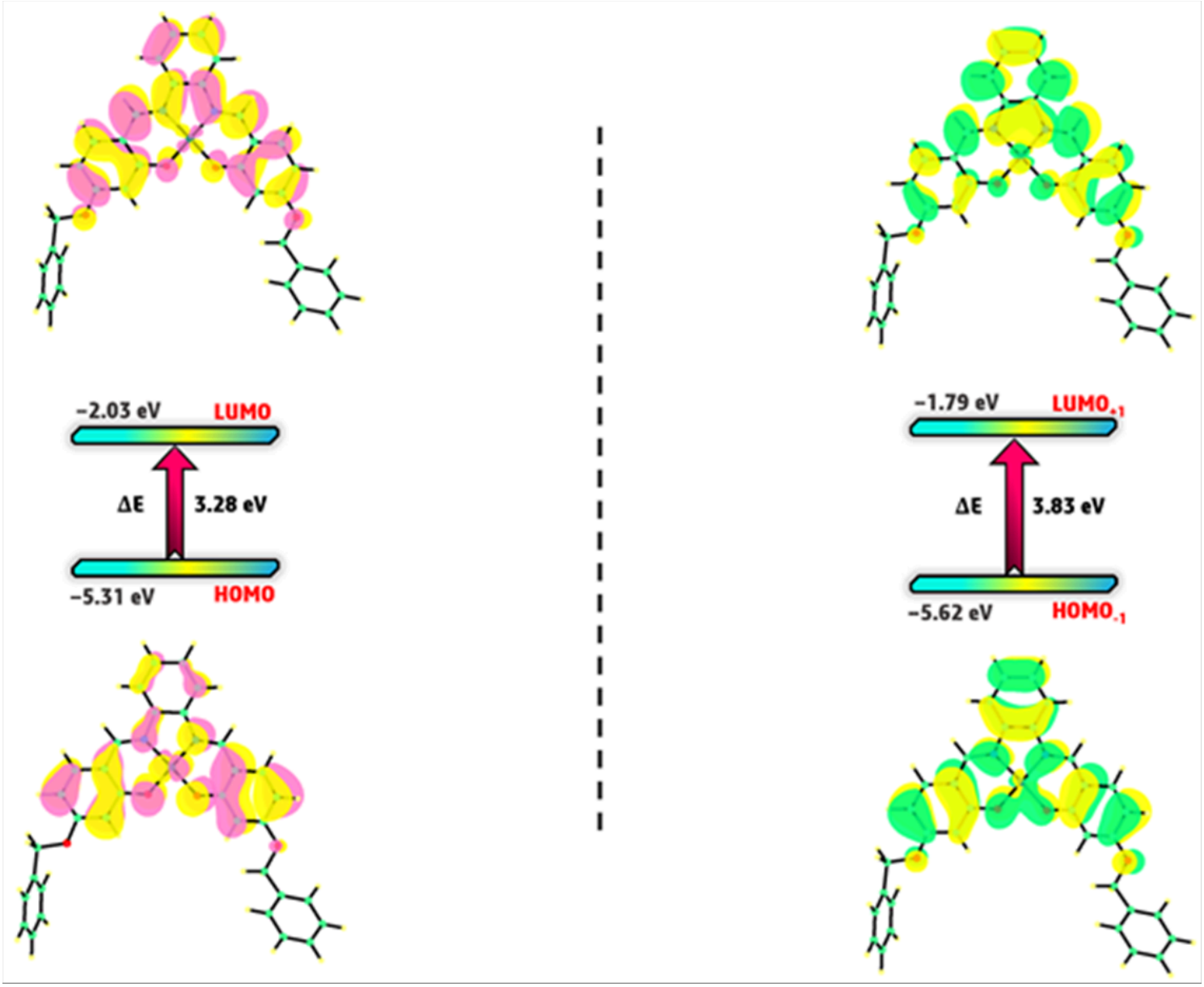


Figure 7

Distributions and energy surfaces of the HOMO, LUMO, HOMO-1, and LUMO+1 of Ni(II) complex.

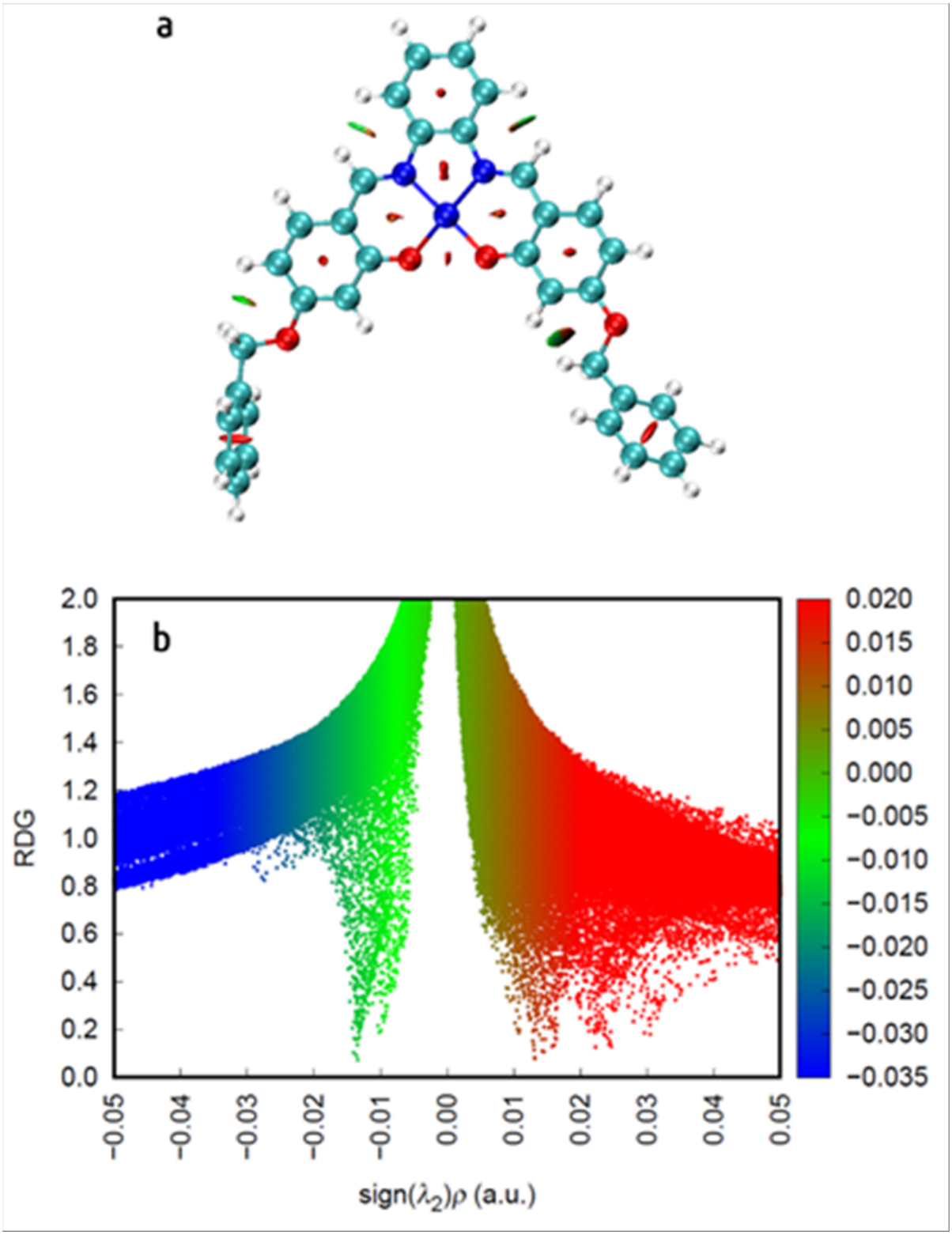


Figure 8

RDG isosurfaces (a) and RDG scatter plot (b) of Ni(II) complex.

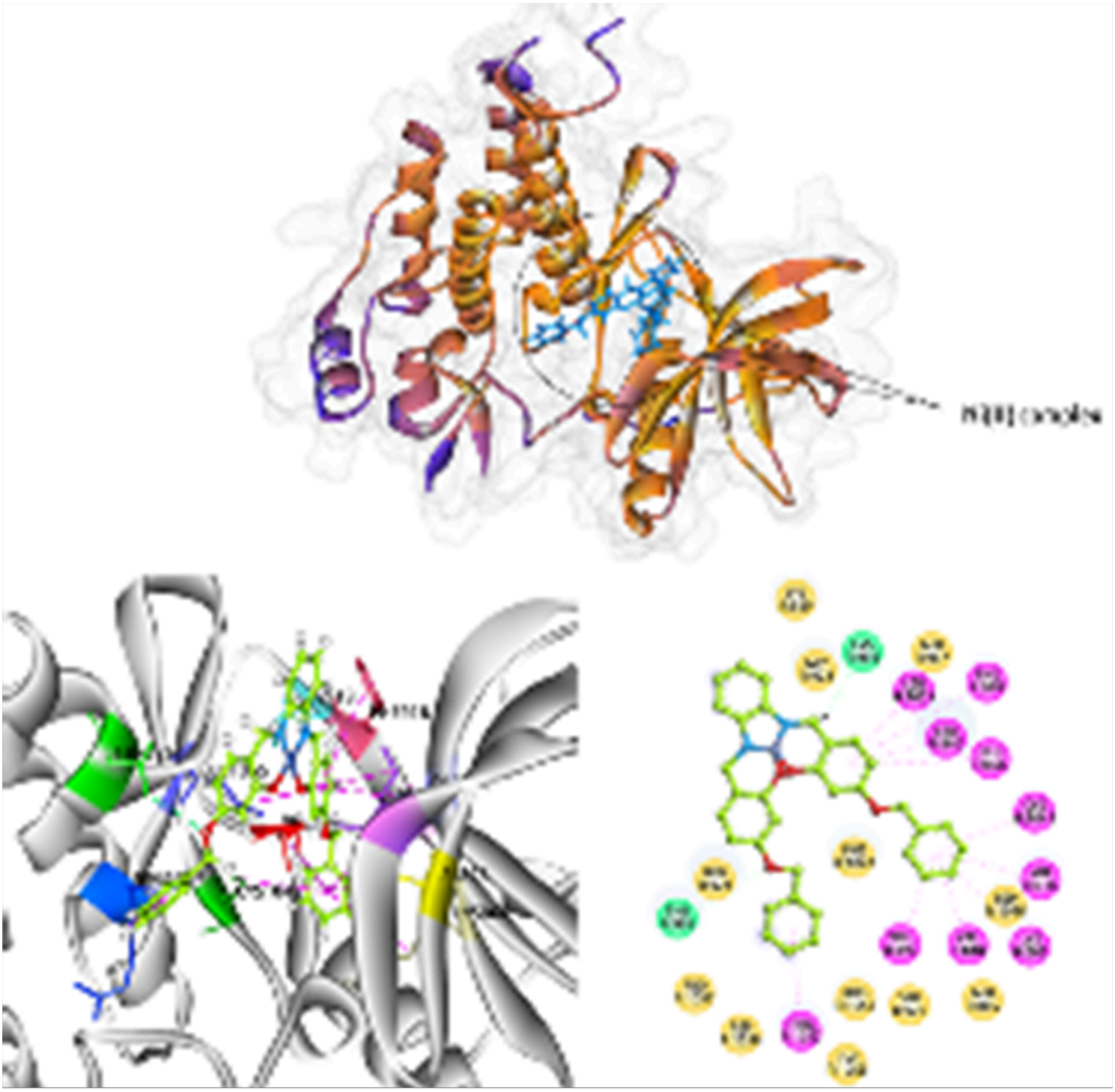


Figure 9

Docking representation of Ni(II) complex against VEGFRTK.

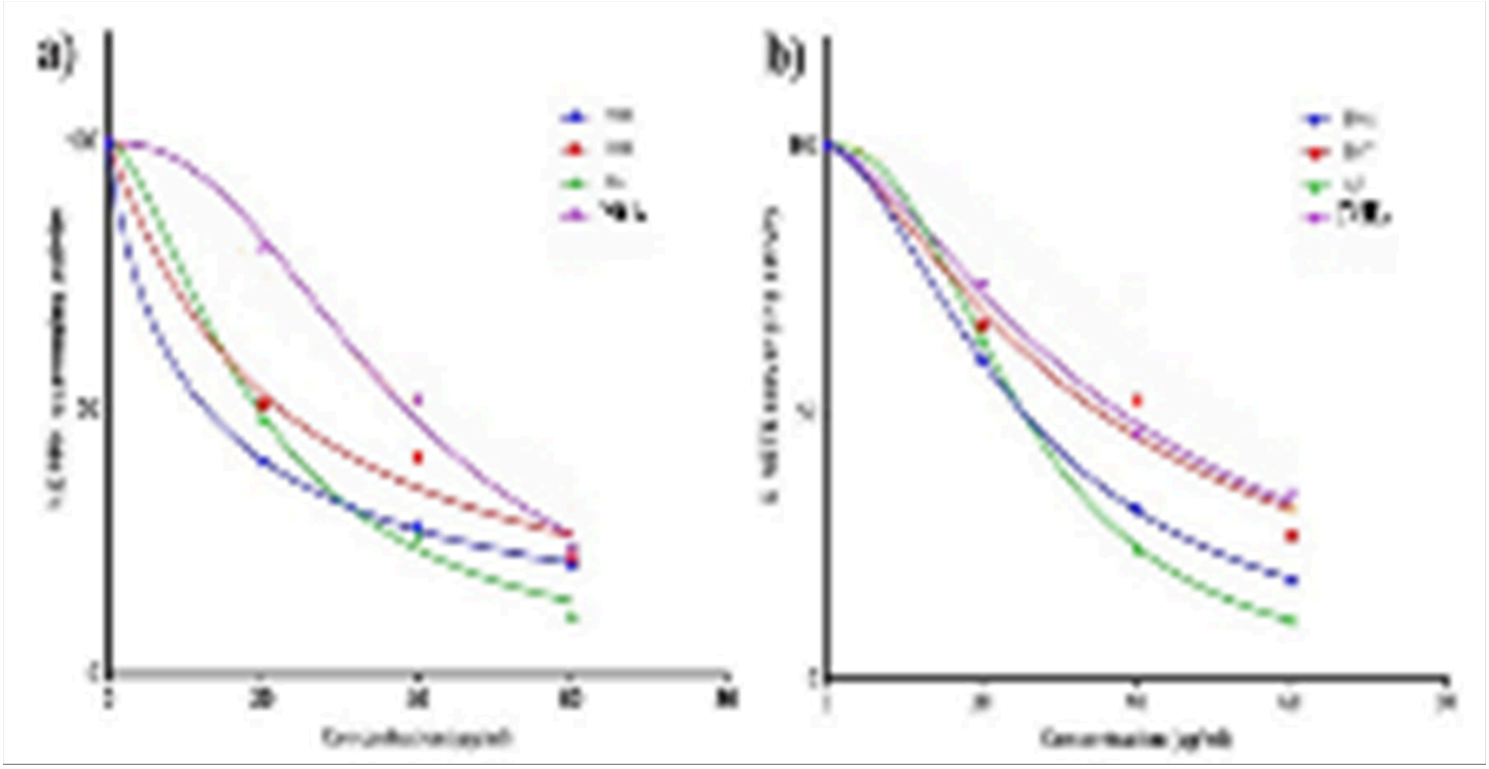


Figure 10

Graphs of antioxidant studies a) DPPH radical scavenging activity and percentages, b) ABTS radical scavenging activity and percentages of the compound **NiL**.

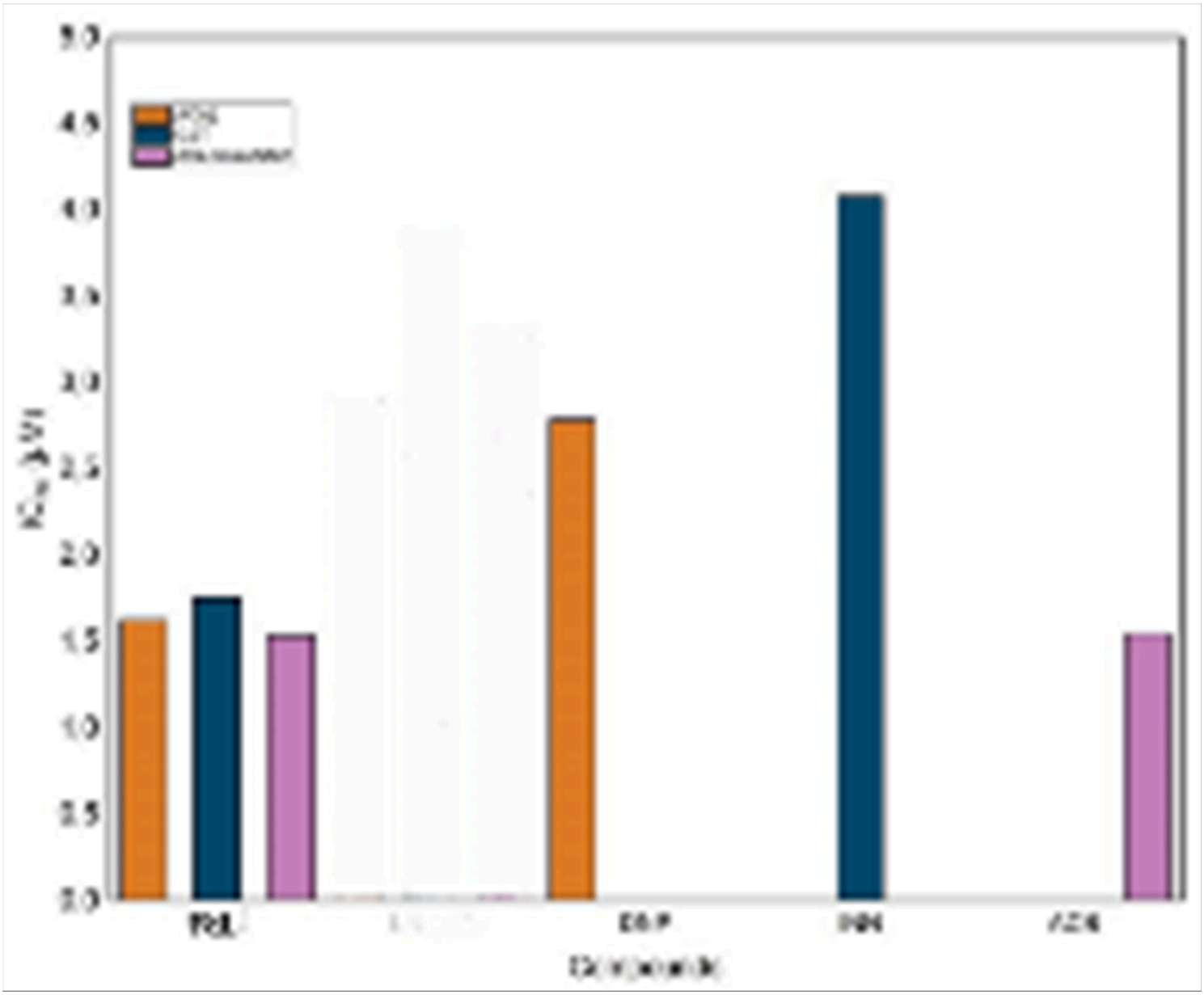


Figure 11

Enzyme-inhibition activity and IC_{50} values of the **NiL**.

Supplementary Files

This is a list of supplementary files associated with this preprint. Click to download.

- supplementaryinformation.docx
- image1.png